Princeton Plasma Physics Laboratory

PPPL- 4515

PPPL- 4515

Progress in Understanding Error-field Physics in NSTX Spherical Torus Plasmas

J.E. Menard, R.E. Bell, D.A. Gates, S.P. Gerhardt, J.-K. Park, S.A. Sabbagh, J.W. Berkery, A. Egan, J. Kallman, S.M. Kaye, B. LeBlanc, Y.Q. Liu, A. Sontag, D. Swanson, H. Yuh, W. Zhu and the NSTX Research Team

May, 2010

Prepared for the U.S. Department of Energy under Contract DE-AC02-09CH11466.

Princeton Plasma Physics Laboratory
Report Disclaimers

Full Legal Disclaimer

Trademark Disclaimer

PPPL Report Availability

Princeton Plasma Physics Laboratory:

http://www.pppl.gov/techreports.cfm

Office of Scientific and Technical Information (OSTI):

http://www.osti.gov/bridge

Related Links:

U.S. Department of Energy

Office of Scientific and Technical Information

Fusion Links

Progress in understanding error-field physics in NSTX spherical torus plasmas

J.E. Menard[1], R.E. Bell[1], D.A. Gates[1], S.P. Gerhardt[1], J.-K. Park[1], S.A. Sabbagh[2], J.W. Berkery[2], A. Egan[3], J. Kallman[1], S.M. Kaye[1], B. LeBlanc[1], Y.Q. Liu[4], A. Sontag[5], D. Swanson[6], H. Yuh[7], W. Zhu[8] and the NSTX Research Team.

[1]Princeton Plasma Physics Laboratory, Princeton, NJ, USA
[2]Columbia University, New York, NY, USA
[3]University of Pennsylvania, Pennsylvania, PA, USA
[4]Culham Centre for Fusion Energy, Culham, UK
[5]Oak Ridge National Laboratory, Oak Ridge, TN, USA
[6]Princeton University, Princeton, NJ, USA
[7]Nova Photonics Incorporated, Princeton, NJ, USA
[8]Credit Suisse, New York, NY, USA

Abstract. The low aspect ratio, low magnetic field, and wide range of plasma beta of NSTX plasmas provide new insight into the origins and effects of magnetic field errors. An extensive array of magnetic sensors has been used to analyze error fields, to measure error field amplification, and to detect resistive wall modes in real time. The measured normalized error-field threshold for the onset of locked modes shows a linear scaling with plasma density, a weak to inverse dependence on toroidal field, and a positive scaling with magnetic shear. These results extrapolate to a favorable error field threshold for ITER. For these low-beta locked-mode plasmas, perturbed equilibrium calculations find that the plasma response must be included to explain the empirically determined optimal correction of NSTX error fields. In high-beta NSTX plasmas exceeding the n=1 no-wall stability limit where the RWM is stabilized by plasma rotation, active suppression of n=1 amplified error fields and the correction of recently discovered intrinsic n=3 error fields have led to sustained high rotation and record durations free of low-frequency core MHD activity. For sustained rotational stabilization of the n=1 RWM, both the rotation threshold and magnitude of the amplification are important. At fixed normalized dissipation, kinetic damping models predict rotation thresholds for RWM stabilization to scale nearly linearly with particle orbit frequency. Studies for NSTX find that orbit frequencies computed in general geometry can deviate significantly from those computed in the high aspect ratio and circular plasma cross-section limit, and these differences can strongly influence the predicted RWM stability. The measured and predicted RWM stability is found to be very sensitive to the $E \times B$ rotation profile near the plasma edge, and the measured critical rotation for the RWM is approximately a factor of two higher than predicted by the MARS-F code using the semi-kinetic damping model.

PACS numbers: 52.55.Fa,52.55.Tn,52.35.Py

1. Introduction

Small deviations from magnetic symmetry can have a large impact on plasma performance in all magnetic confinement systems. For example, high toroidal mode number (high-n) ripple can impact both fast and thermal ion confinement in tokamaks, and recent experiments on JET and JT-60 [1] have shown significant improvements in H-mode confinement and achievable beta when ripple is reduced. Potentially more deleterious losses of magnetic symmetry occur when low-to-intermediate n=1-3 resonant and non-resonant error fields are present. Such fields are commonly caused by imperfections in the magnetic field coils providing the confining magnetic field. These magnetic "error-fields" can induce locked magnetic islands at low density and/or low plasma rotation [2, 3, 4, 5, 6], can be amplified by the plasma at high beta [7], and can induce plasma flow damping via neoclassical toroidal viscosity (NTV) [8, 4, 9], potentially leading to rotation collapse in scenarios where the RWM is stabilized by the plasma rotation. In this article, we describe the results of systematic studies on the low-aspect-ratio NSTX device related to the detection, correction, and improved understanding of low-n magnetic error fields. Section 2 describes NSTX experimental results. These results include a description of sources, detection, and correction of intrinsic error fields in Section 2.1, low-β locked-mode threshold scalings in Section 2.2, high-β_N error field correction and pulse-extension in Section 2.3, and RWM stability threshold physics in Section 2.4. Section 3 provides a summary of these results.

2. Experimental Results

The detection and correction of small ($< 0.1\%$) low toroidal mode number (low-n) deviations from axisymmetry can significantly improve plasma performance. Early in the operation of NSTX, the detection and correction of n=1 error fields generated

by the primary vertical field coils enabled stable operation at low density without mode locking [10]. Subsequently, sustained high-beta operation was routinely achieved; however rotation decay during the discharge was still commonly observed. More recently, two additional smaller error fields have also been detected and corrected enabling further significant improvements in plasma performance.

2.1. Detection and correction of static error fields and low-frequency instabilities

Effective error field (EF) and resistive wall mode (RWM) control relies heavily on the robust detection of small (of order 1 Gauss) non-axisymmetric magnetic fields. NSTX has implemented extensive low-frequency mode detection capabilities including 54 sensors measuring two components of the non-axisymmetric magnetic field. As illustrated in Figure 1, the NSTX sensor array consists of 24 radial (BR) and 24 poloidal (BP) sensors mounted in-vessel on the primary passive plates plus 6 mid-plane ex-vessel BR saddle coils. The in-vessel array measures fields above and below the mid-plane with toroidal mode-numbers n=1, 2, 3, while the mid-plane array is configured to detect only n=1 fields. All BR and BP magnetic field signals from these sensors shown in subsequent figures are computed by dividing the measured magnetic flux by the sensor area. The mid-plane external active control coils are also shown in Figure 1.

The NSTX low-frequency mode detection system has been instrumental in identifying vacuum error fields. Recently, the 30 radial field sensors have been utilized to identify an n=1 EF resulting from a small displacement of the central toroidal field (TF) coil bundle. As illustrated (in an exaggerated fashion) in Figure 2, the TF coil exhibits a predominantly tilting motion and is approximately fixed at the bottom of the machine. For reference, the TF rod displacement at the horizontal mid-plane inferred from the in-vessel BR magnetic sensors is approximately 2mm, or 1/1000 of the largest

diameter vertical field coil of NSTX (PF5). Additional analysis of the coil lead areas of NSTX indicates that an electromagnetic interaction between the ohmic heating (OH) coil leads and the TF is responsible for motion of the TF central rod relative to the vacuum vessel and poloidal field (PF) coils of NSTX.

An important clue in identifying the EF resulting from TF coil motion was the observation that the EF is only present when the TF and OH coils are energized simultaneously. Figures 3a and b show the TF and OH coil current waveforms typical of 0.75MA beam-heated plasmas in NSTX. As shown in Figure 3c, the upper in-vessel BR array measures a 4 to 6 Gauss error field roughly proportional to the magnitude of the OH coil current during the flat-top phase of the TF current. In this figure, the sensor signals resulting from the individual OH and TF coil currents has been subtracted off, indicating that this field must result from a non-linear source. Additional BR measurements at different TF currents indicates that the EF is roughly proportional to $I_{OH} \times I_{TF}$ consistent with an electromagnetic interaction between the coils. However, as is also evident in Figure 3b-c, there is also significant temporal lag (100-200ms) between the zero-crossing of the OH current and the time of minimum EF. In addition to this time delay, the magnitude of the EF depends on OH current polarity. Following the discovery of these OH×TF error fields, mechanical shims were placed between the TF coil and the tension-tube on which the OH coil is wound in an attempt to reduce the motion of the TF coil. Figure 3c shows that the EF pre-shim (blue) is comparable to that obtained post-shim (red) when the OH coil is at high current, but the shimming does appear to reduce and/or delay the error field for times when the OH current is between 0 and -10kA. As shown in Figure 3d, the toroidal angle of the EF changes by 150° instead of 180° when the OH current changes sign. Improvements to the OH coil lead area could reduce the TF displacement by an estimated factor of 2-4 and are under

consideration.

The deviations of the EF from being simply proportional to $I_{OH} \times I_{TF}$ shown in Figure 3 may be the result of the thermal expansion of the TF and/or OH coils during their operation. Results such as these highlight the potential importance of EF sources resulting from thermal expansion and mechanical motion in large future burning plasma devices such as ITER.

Because of the need to estimate the vacuum EF source for locked-mode studies and EF correction, a model has been developed to estimate the OH×TF EF. The model includes both shift and tilt of the TF center rod. The outer TF return legs are assumed to be fixed, as any movement of the TF center rod is taken up by vacuum bellows and flexible current carrying jumpers between the center-stack and outboard support structure. In the model, the TF coil system is represented as 12 filamentary coils as shown Figure 4, and 1 millimeter shifts and tilts are applied to the central TF conductors in 2 orthogonal directions for each type of coil motion. The model employs single-pole low-pass time filtering to account for time delay and includes both the signed and absolute value of $I_{OH} \times I_{TF}$ to account for the polarity dependence of the EF. Thus, the 4 fictitious TF error-field producing coils corresponding to the 4 coil motion degrees of freedom have coil currents with the following functional form:

$$I_k = c_{1k} LPF(I_{OH} I_{TF}) + c_{2k} |LPF(I_{OH} I_{TF})| \quad (1)$$

where $k = 1 - 4$ is the index of the error-field-producing model TF coil and "LPF" corresponds to a causal low-pass filter operator with a time-constant of 0.1s. The coefficients c_{1k} and c_{2k} are chosen by a least-squares fitting error minimization process comparing the model and the measured n=1 error field at the BR sensors. As shown in Figure 5a, the model EF is in good agreement with the experimentally measured EF for OH current waveforms that are sufficiently short in duration ($\leq$0.7s) as is typically

the case for ohmically-driven plasmas typical of locked-mode experiments described in Section 2.2. However, Figure 5b shows a larger (several Gauss) discrepancy between the model and measured EF when the OH current waveforms are significantly longer in duration. As a result, pre-programmed n=1 EF correction has generally proven to be more difficult in high-β long-pulse H-mode discharges in NSTX, and as a result, minimization of resonant field amplification (RFA) via active feedback control is now commonly relied upon for suppressing n=1 error fields as described in Section 2.3.

2.2. Low-β locked-mode threshold scalings

Low-n error-fields can be particularly problematic at low-density where the plasma $\vec{E} \times \vec{B}$ and/or diamagnetic rotation is often insufficient to shield out the magnetic islands naturally induced by resonant magnetic perturbations [11, 12, 13, 14, 15, 16]. A determination of the scaling of the error field magnitude that triggers core non-propagating (in the lab frame) magnetic islands, or "locked modes", is important for both low aspect ratio and standard aspect ratio tokamaks including ITER. Such scaling studies remain necessary, as a first-principles theory consistent with measured locked-mode threshold scalings [2, 3, 4, 5, 6, 17] has not yet been fully developed. However, the inclusion of drift-MHD and semi-collisional effects [14, 16] in addition to non-resonant magnetic braking effects [18, 19] can alter the predicted scaling in important ways and potentially improve the agreement between experiment and theory.

NSTX and MAST locked mode (LM) studies provide a strong test of locking threshold theories by extending the experimental parameter regime to lower aspect ratio (A $\approx$ 1.5 versus 3) and correspondingly much stronger edge magnetic shear. As shown in Figure 6 (reprinted from Figure 10 of Reference [6]), ST data also extends the existing locked-mode database to lower magnetic field for scaling studies for ITER and

provides guidance on the error-field correction requirements for future ST devices [20].

To determine the n=1 locked mode threshold, an n=1 external error field was applied using the non-axisymmetric field coils shown in Figure 1. The applied field was ramped linearly in time as shown in Figure 7a and starting at time when the minimum safety factor value was in the range of 1.4 to 2 and reaching maximum current before the q=1 surface entered the plasma. On selected shots, short (50ms) neutral beam injection (NBI) pulses were used during the n=1 field ramp to enable Motional Stark Effect (MSE) measurements of the safety factor profile. These measurements confirm that the q profiles obtained with magnetics-only equilibrium reconstructions were consistent to within $\Delta q = \pm 0.4$ with reconstructions obtained with internal pitch-angle constraint from MSE. Plasma rotation profile measurements were not generally available for these low-density ohmic locked-mode discharges, so no direct assessment of the roles of $\vec{E} \times \vec{B}$ or diamagnetic rotation on the mode locking process is possible.

Locked modes excited during the n=1 field ramp were detected as shown in Figure 7b using the magnetic sensors shown in Figure 1. For the locked-mode threshold analysis, the OH×TF EF model described in Section 2.1 was used to estimate the intrinsic EF in the calculation of the total error field. Scans of the locking threshold as a function of toroidal angle of the applied n=1 field confirmed that the model EF toroidal phase angle is in good agreement with experimentally determined phase angle. During most of the subsequent parameter scans used for determining the locking threshold, the applied EF phase was aligned with the intrinsic (OH×TF) EF phase. This increases the total n=1 field that can be applied and increases the density for which locked modes can be excited and locking thresholds determined in the experiment. The range of line-average electron densities scanned varied by a factor of 4 from 0.5 to $2 \times 10^{19} \mathrm{m}^{-3}$. The vacuum toroidal field at the plasma geometric center was also varied by nearly a factor

of 2 ranging from $B_{T0} = 0.3$ to 0.55 Tesla.

The NSTX locked-mode experiments and analysis differ from previous tokamak efforts in several important ways. First, previous locked-mode threshold experiments were commonly performed with q(0) near or below 1 and often include sawtoothing discharges, whereas the NSTX experiments did not have the q=1 surface in the plasma and therefore focus on the formation of locked modes at integer q surfaces ≥ 2. Second, the large difference between the cylindrical kink safety factor q^* [21] and near-edge safety factor q_{95} (q at 95% normalized poloidal flux) at low aspect ratio makes it unclear which if any global q parameter can represent q profile effects in the locking threshold scaling across a range of aspect ratio. Thirdly, and most importantly, the Ideal Perturbed Equilibrium Code (IPEC) [22] has demonstrated that plasma response effects including poloidal mode coupling and field amplification are important in quantitatively determining the penetration threshold and optimal correction of error fields. In particular, IPEC can compute the perturbed singular currents responsible for shielding the external error field at low-order-rational surfaces. Because of plasma response effects, the total (plasma + vacuum) resonant field perturbations computed by IPEC can differ significantly from the resonant vacuum fields.

The locked-mode threshold is commonly expressed as a dimensionless ratio:

$$B_r(lock)/B_T \propto \bar{n}_e^{\alpha_n} {B_T}^{\alpha_B} q^{\alpha_q} {R_0}^{\alpha_R} \tag{2}$$

where $B_r(lock)$ is the magnitude of the resonant field at the q=2 surface at the onset of error field penetration leading to mode locking, $\bar{n}_e$ is the line-average electron density, B_T is the vacuum toroidal field at the plasma geometric center R_0, and q is the magnetic safety factor (or a parameter related to the magnetic shear). The range of R_0 values in the NSTX locked-mode experiments is sufficiently small ($< 10\%$ variation) that plasma radius is not included in the NSTX locked-mode threshold fits. The magnetic field

$B_r(lock)$ is commonly defined as the m=2, n=1 component of the Fourier-decomposed straight-field-line coordinate flux-surface-normal vacuum magnetic field at the q=2 surface [6] in which the 3D vacuum perturbed field is superposed on the 2D equilibrium field. Mathematically, $B_r(lock) = |\delta B_{2,1}|$ where:

$$\delta B_{m,n} \equiv \frac{1}{(2\pi)^2} \oint e^{i(n\phi - m\theta)} \delta \vec{B} \cdot \frac{\nabla \psi}{|\nabla \psi|} d\theta d\phi, \tag{3}$$

$\delta \vec{B}$ is the non-axisymmetric field perturbation, ψ is the equilibrium poloidal flux, θ is the poloidal angle coordinate, ϕ is the toroidal angle coordinate in cylindrical coordinates, the 2D equilibrium magnetic field $\vec{B} = \nabla\psi \times (\nabla\phi - q(\psi)\nabla\theta)$, and the magnetic safety factor $q(\psi) \equiv \oint \frac{\vec{B}\cdot\nabla\phi}{\vec{B}\cdot\nabla\theta} \frac{d\theta}{2\pi}$.

It is important to note that the spectral amplitude of the perturbed normal field depends on the choice of Jacobian [23], and therefore the perturbed normal field is not invariant with respect to even small changes in flux surface shape or for plasmas of different aspect ratio. However, the spectral amplitude of the perturbed island width is independent of choice of Jacobian [23], as are therefore the perturbed poloidal and helical fluxes [24]. Thus, area-weighted and normalized fields should in general be used for comparing resonant field amplitudes. The area-weighted perturbed field $\delta B^{aw}_{m,n}$ is defined as the ratio of the resonant perturbed flux $\delta\Phi_{m,n}$ to the flux surface area $A_{surface}$:

$$\delta B^{aw}_{m,n} \equiv \frac{\delta\Phi_{m,n}}{A_{surface}} = \frac{\frac{1}{(2\pi)^2} \oint e^{i(n\phi - m\theta)} \delta\vec{B} \cdot \nabla\psi J d\theta d\phi}{\oint |\nabla\psi| J d\theta d\phi} \tag{4}$$

where the Jacobian $J \equiv (\vec{B} \cdot \nabla\theta)^{-1}$ and all quantities are evaluated at the resonant magnetic surface of interest. When resonant normal magnetic fields are utilized in subsequent scalings and figures, unweighted fields are computed using Equation 3 and area-weighted fields are computed using Equation 4.

Since the integrated perturbed resonant electromagnetic ($\delta\vec{J} \times \delta\vec{B}$) torque in the vicinity of the singular layer induced by the externally applied 3D field scales as the square of the perturbed flux [12], it can be expected that that the usage of area-weighted

perturbed fields will also be important in comparing locked-mode thresholds across experiments. Further, the perpendicular viscous torque (anomalous or collisional) is generally taken to be independent of the perturbed field amplitude, whereas the parallel neoclassical toroidal viscosity (NTV) in the bulk plasma is proportional to the square of the perturbed magnetic field strength on the perturbed (3D) flux surfaces and can effectively enhance the perpendicular viscosity [18]. For the reasons described above, the locked-mode scalings that follow will use an area-weighted (flux-like) definition of the perturbed normal magnetic field unless otherwise noted.

Before discussing the impact of plasma response effects and perturbed field representation in the locking data, it is important to attempt to understand the role of safety factor and magnetic shear in the locking data, especially since the low-aspect-ratio low-density locked mode experiments for MAST [20] and NSTX generally have significantly higher q_{95} = 5-13 than at conventional aspect ratio (q_{95} = 3-5) [25]. In most locking threshold experiments, the scaling exponent for q_{95} has generally ranged from near zero to positive [25, 20] with the exception of C-Mod data in which the exponent was found to be negative ($\alpha_q \approx -0.6$). Like the C-Mod data, using the vacuum field perturbation scaling, the NSTX locking data also exhibits a negative exponent ($\alpha_q \approx -0.7$) if the density scaling exponent is constrained to be $\alpha_n = 1$. Figure 8 shows the best fits to the NSTX locking data using simultaneous fits of the density, magnetic field, and magnetic safety factor and global shear for each locking case. As shown in Figure 8a, the fit to the locking data with these parameters using q_{95} as a magnetic safety factor variable is good with an overall fitting ratio and uncertainty of 1.02 and 10% respectively (bottom-most plot with the data samples ordered by increasing density). Tests of magnetic shear variables including internal inductance and local q-shear yield similarly good fitting results for the vacuum locking data. These scaling results imply

that magnetic shear rather than edge q (q_{95}) could be an important physics parameter for locking when utilizing the vacuum locking data. A magnetic shear related parameter that could potentially be useful for a range of aspect ratios is internal inductance l_i, and Figure 8b shows that the magnitudes of the density and magnetic field exponents are reduced somewhat with l_i used as a magnetic shear variable, and a positive correlation between locking threshold and l_i is observed with $\alpha_q \approx 0.5$. Similar scaling coefficients are obtained if the local magnetic shear $\frac{dq}{d\rho}\big|_{q=2}$ or $\frac{dq}{d\rho}\big|_{q=3}$ are used as shear parameters.

It is also noteworthy that for all the fits described above using the vacuum perturbed magnetic field, the locking scaling exponents depend only weakly on which magnetic surface (q=2 or 3) the scalings are based upon. Thus, this scaling data does not provide an indication of which mode-rational surface dominates the locking process. For the NSTX data, the q=2 surface can be located at much smaller minor radius than the q=3 surface since the minimum q is well above one. Thus, the q=3 (or higher) surface could in principle be in a region of increased applied error field and may dominate the locking process. For this reason, locking coefficients at both the q=2 and q=3 surfaces are computed in the analysis that follows.

Moving beyond vacuum representations of the perturbed magnetic field, previous IPEC calculations have shown that the total resonant field perturbation is most strongly correlated with the locked-mode threshold as a function of plasma density, and that the total resonant field is needed to explain error-field correction results on NSTX and DIII-D [26]. For the mode-locking analysis using the IPEC-computed total resonant perturbed field, inversely proportional scalings of the threshold with q_{95} and proportional scalings with internal inductance are again observed similar to the trends observed in the vacuum perturbed field scalings. However, important differences between the vacuum superposition and IPEC total field scalings are observed when comparing the fits to the

q=2 versus the q=3 data. Using l_i as a magnetic shear variable, fits with significantly lower fitting error are observed for locking at q=3, and the density scaling exponent is also closer to unity for assumed dominant locking at q=3. In contrast, as shown in Figure 9a for locking at q=2, the density scaling exponent $\alpha_n \approx 0.77$ is well below unity and the overall error in the fit (bottom plot) is twice as high (0.22 versus 0.11) as that obtained for the vacuum field scalings. As is evident from these fits, much of the increase in fitting error is attributable to the poor fit at reduced magnetic field and high internal inductance. Importantly, even if the fitting outlier at low toroidal magnetic field is removed from the fitting process, a positive magnetic field exponent is obtained in the fits. In contrast, Figure 9b shows that locking scalings using the local shear at the q=2 surface have a density scaling closer to linear and markedly reduced error in the scaling exponents and in the overall fit using the local magnetic shear. The magnetic field scaling exponent is again negative, consistent with all other previously published field scalings and in contrast to the positive field exponent if l_i is used as a magnetic shear variable. This finding suggests that the inclusion of local plasma response effects computed by IPEC can help determine which physical parameters are most relevant to the mode-locking physics - in this case the local magnetic shear at low-order rational q surfaces in the plasma core.

In light of some important differences between the IPEC and vacuum superposition results for the locked-mode scalings, and given the differences between the area-weighted perturbed field and non-weighted field used elsewhere, it is important to consider the dependence of the locked-mode scalings on the definition of the perturbed radial magnetic field and/or perturbed flux. Figure 10 shows the NSTX locked-mode scaling exponents and their uncertainties for IPEC calculations of the total resonant normal B-field (area-weighted) including plasma response (green), the vacuum resonant normal

B-field (area-weighted) (red), and the vacuum resonant perturbed normal B-field (non-area-weighted) (blue) all computed at the q=2 and q=3 surfaces. Scaling exponents and uncertainties at q=2 from Alcator C-Mod are also shown in orange for comparison, and theoretical predictions from recent locking theory including NTV damping [18] are indicated by the dashed lines. As is evident from the figure, NSTX data shows an approximately linear density scaling and inverse toroidal field scaling broadly consistent with higher aspect ratio (and higher magnetic field strength) tokamaks. As shown in Figure 10a all the NSTX density scaling exponents are somewhat below unity, with the vacuum resonant perturbed normal B-field (blue) the smallest in magnitude. As shown in Figure 10b, all the magnetic field scaling exponents are substantially smaller in magnitude than the Cole theory value of α_B = -1.3 [18]. The IPEC α_B coefficients are small and approach zero for q=2 and may be the result of potentially important geometrical and plasma response effects such as enhanced poloidal mode coupling at reduced aspect ratio. Further, as described above, the usage of IPEC total resonant field most strongly impacts the magnetic shear scaling exponent as shown in Figure 10c for q=2. The density and field scaling exponents can be used to compute a size scaling exponent $\alpha_R = 2\alpha_n + 1.25\alpha_B$ assuming Connor-Taylor invariance [27] applicable to the quasi-neutral high-beta Fokker-Planck plasma model for ohmically heated plasmas [28]. Since there is some uncertainty in the location of the q=2 and 3 surfaces, and since multiple m $\geq$ 2 locked islands may be present in the experiment, the average q=2 and q=3 exponents are computed. The vacuum superposition non-area-weighted exponents are $\alpha_n = 0.73, \alpha_B = -0.50, \alpha_R = 0.84$, the vacuum superposition area-weighted exponents are $\alpha_n = 0.91, \alpha_B = -0.94, \alpha_R = 0.64$, and the IPEC-derived area-weighted coefficients are $\alpha_n = 0.90, \alpha_B = -0.37, \alpha_R = 1.34$.

An important application of the locking scalings described above is the estimation

of error field thresholds for ITER, and therefore the error field correction requirements and coil fabrication and installation tolerances. Overall, for the exponents discussed above, the IPEC-derived exponents have the least negative α_B and the most positive α_R and are therefore the most favorable for ITER. Figure 11 compares the projected locking threshold for ITER for the non-area-weighted vacuum superposition field (blue) and area-weighted vacuum superposition field (red) and the area-weighted IPEC total field (green) using local shear at the q=2 surface (Figure 11a) and at the q=3 surface (Figure 11b) as magnetic shear variables in the locked-mode threshold fitting. For the variation of field models and q surfaces chosen, there is up to a factor of 10 variation in the projected locking threshold for ITER. Importantly, as seen in Figure 11b, the area-weighted vacuum superposition and IPEC total fields generally project to the most pessimistic locking threshold and are systematically lower than the commonly used non-area-weighted vacuum field. This finding motivates revisiting the locking projections for ITER from other devices and extending them to include both geometrical and plasma response effects. Previous error-field correction requirement calculations for ITER used an empirical three-mode model for the locking threshold and specified that ITER be able to correct any intrinsic n=1 error fields to residual normalized amplitudes $\delta B_r/B_T$ no larger than 0.5 Gauss / Tesla [29]. Even for the least favorable NSTX scaling to ITER including plasma response effects, the minimum threshold $\delta B_r/B_T$ = 1 to 5 Gauss / Tesla is 2 to 10 times higher than the minimum EF correction capability of ITER, which is a favorable result.

The NSTX locking results are obtained at aspect ratio A $\approx$ 1.5 which is approximately half the ITER value A $\approx$ 3. When the locking threshold scaling expression of Equation 2 is extended to include aspect ratio and σ_{NR} (the ratio of the non-resonant to resonant error field at the resonant surface [18]), and preliminary scaling fits are

performed including NSTX data and conventional aspect ratio tokamak data from DIII-D and C-Mod, regression analysis finds that the threshold exhibits little correlation with aspect ratio and weak inverse dependence on σ_{NR}. Thus, in future work, multi-machine locked-mode threshold scaling expressions for extrapolation to ITER may need to be revised to take into account the effects of non-resonant torques and the plasma response effects described here, and also account for the multiple operating scenarios proposed for ITER [30].

2.3. Error field correction and plasma sustainment at high beta

2.3.1. n=1 error field detection and correction The locked-mode experimental results described in Section 2.2 indicate that the intrinsic OH×TF error field of NSTX is sufficiently small that additional n=1 error field is commonly needed to trigger mode-locking except at the very lowest operating densities of NSTX. At the lowest densities shown in Figure 8 ($\bar{n_e} \leq 5 \times 10^{18} m^{-3}$ and normalized density $f_{GW} \equiv n_e/n_{Greenwald} \leq 0.1$ [31, 32]) runaway electron formation during plasma disruption has also been observed, so very low density regimes are generally avoided except during locked-mode experiments and some radio-frequency heating and current-drive experiments [33].

However, at higher plasma beta, in particular above the ideal kink no-wall instability limit, resonant field amplification (RFA) of the n=1 intrinsic error field can substantially increase the field inside the plasma and lead to plasma rotation damping from NTV [9]. For NSTX, this plasma rotation damping commonly occurs as the OH current increases in amplitude later in the plasma pulse and when operating above the no-wall limit and is correlated to the appearance of resistive wall modes [34, 35] as shown in Figure 12. The black curves in Figure 12a-d illustrate that operation above the no-wall instability limit can lead to a collapse of the plasma beta (a), followed by a

plasma current disruption (b) induced by the large n=1 field perturbation (d) measured by the upper poloidal field array of Figure 1.

Figure 12e shows that between 0.470s and 0.480s the plasma rotation (as measured using impurity carbon 6^+ charge exchange spectroscopy [36]) at large minor radius and near the q=2 and 3 surfaces is damped as the n=1 mode grows to approximately 10 Gauss in amplitude as shown in Figure 12d. During this early phase as the rotation is being damped but still remains near its initial value, the plasma beta (and hence confinement) remains near its initial value and above the no-wall instability limit. However, between 0.480s and 0.490s the plasma rotation has decreased to near zero at large minor radii and the mode amplitude has grown 3-4 times larger. During this large mode amplitude phase the thermal confinement is lost and the beta collapses to 20% of its original value. The mode persists through the remainder of the discharge despite the reduction of the normalized beta far below the no-wall limit. Because of the mode-induced confinement degradation, the loop voltage required to maintain the plasma current increases by a factor of 10 to 20 and the plasma current disrupts shortly thereafter when the OH coil current limit is approached and sufficient positive loop voltage to sustain the plasma can no longer be applied.

In contrast, the red dashed curves of Figures 12a-d show the effect of the addition of a time-evolving n=1 applied field with toroidal phase opposite to that of the calculated intrinsic error field and an amplitude chosen to be linearly proportional to the intrinsic error field amplitude and optimized to minimize toroidal flow damping. With this method of error field correction (EFC), n=1 mode growth and beta and current disruption can be delayed and/or avoided. The optimal proportionality coefficient for correction was empirically determined and based primarily on cancellation of the m=0 component of the vacuum perturbed helical flux at the q=2 surface, with a small

contribution from the m=2 component also required [37]. As shown in Figures 12f, the sustainment of high plasma beta is correlated with the avoidance of plasma rotation damping and the sustainment of high plasma rotation across the plasma.

Calculations of the OH×TF error field were implemented in the plasma control system (PCS) [38] to provide a real-time signal for a "predictive" error-field correction (PEFC) algorithm to reduce the plasma rotation damping and improve sustainment of high beta. Figure 13 shows a comparison of discharge parameters with (black) and without (red) PEFC. As seen in the figure, the duration of operation above the no-wall stability limit was increased by 60-70% through the application of PEFC and the duration of sustained high rotation was similarly increased.

Real-time calculations of the mode n=1 poloidal field amplitude and phase were also implemented and utilized to enable tests of active feedback suppression of n=1 RFA and RWMs [39]. Scans of the relative phase between the measured plasma n=1 poloidal field and the mid-plane radial field applied by the RWM/EF coils were performed to optimize the RFA/RWM suppression and sustainment of high plasma beta. The proportional gain G_P was also scanned, and the highest stable gain was $G_P \approx 0.7$. Here the G_P is such that $G_P = 1$ when the n=1 plasma mode field at the B_P sensors is equal in magnitude to the vacuum field from the coils also measured at the B_P sensors. Significantly higher gain increased the probability of n=1 feedback system instability and plasma disruption (likely due to the large n=1 fields applied). For feedback gain $G_P \approx 0.7$ the feedback system alone was not reliably able ($\approx$ 50% success rate) to suppress n=1 RFA or to extend the pulse duration substantially beyond the performance of the PEFC algorithm. The combination of PEFC and n=1 active feedback control to form a "dynamic" error field correction (DEFC) algorithm was successful in substantially increasing the duration of high plasma beta. As is evident from Figure 13, with DEFC the duration of plasma

operation above the no-wall instability limit was more than doubled and the plasma rotation near the q=2 and 3 surfaces is sustained until nearly t=1s.

In the later phases of these discharges (t > 1s), the plasma can also become unstable to fast rotating MHD instabilities (5-20kHz) including neoclassical tearing modes NTMs [40] or saturated kink [24] and interchange modes [41] which can also slow the plasma rotation, degrade confinement, and sometimes cause disruption. The DEFC system has insufficient bandwidth to respond to these instabilities, and these instabilities are best avoided through changes/increases in core safety factor and/or increases in shaping factor [42].

Additional scans were performed to understand the importance of fast feedback in the EFC experiments. In the blue curves in Figure 13, EFC coil currents were pre-programmed to match the time-smoothed evolution of the EFC coil currents during DEFC. As seen in the figure, the sustainment of high plasma beta and rotation is nearly identical for the pre-programmed EFC and DEFC controlled plasmas. Since NSTX RWM instabilities typically have growth rates of 1-10ms [39], this result indicates that for these plasmas with only optimized pre-programmed EFC and no active feedback control, there are no unstable n=1 RWMs. Thus, we infer the DEFC system is suppressing RFA (i.e. field amplification by a marginally stable RWM) rather than unstable RWMs directly.

Importantly, Figure 13c shows that the DEFC system does modify the correction coil currents relative to the PEFC alone, and that this has important consequences for plasma performance. The direct measurement of plasma response to the intrinsic EF provided by the real-time n=1 BP measurement can modify the time evolution of the amplitude of applied correction field, change its peak value by 20-30%, and modify the optimal correction phase by 10-20 degrees. This result is perhaps not surprising, given

that variations in the evolution of q(r,t) and beta can modify the plasma response to the OH×TF error field and hence RFA and NTV damping of plasma rotation.

A significant part of the (initial) inability to utilize n=1 active feedback control alone for DEFC resides in the uncertainty of the amplitude and phase of the measured n=1 plasma response. Part of this uncertainty arises from imperfections in the sensor gains and positions [35]. For example, in addition to compensation of direct vacuum pickup from all the poloidal field coils and toroidal field coils, the RWM/EF sensors are also prone to pickup of AC currents in passive conducting structures of NSTX and from the plasma current itself. While compensation of this pickup is included in off-line analysis of the mode signals, only the DC contribution is generally included in real-time calculations, since AC contributions are generally small for slowly evolving plasmas with sufficient rotation to suppress unstable RWMs. Thus, the measured plasma response is generally some combination of the actual plasma response to n=1 error fields and offsets from imperfect compensation of all other vacuum sources of apparent mode field. As a result, it is not uncommon to have 1-5 Gauss of residual measured mode amplitude during plasma operation even when no unstable low frequency mode is present. Additional reductions in the residual offset n=1 field are achieved by "re-zeroing" the sensor signals during the plasma current flat-top at a time when the OH×TF EF is expected to be small and (if possible) before the plasma beta exceeds the no-wall limit (to minimize the effects of RFA). This "re-zeroing" was utilized for the DEFC shots of Figure 13 and was essential to the achievement of increased duration of operation above the no-wall limit.

Following the addition of shims to the TF coil bundle to reduce the intrinsic error field, the error field was reduced, but the amplitude of the error field was further from being simply proportional to the time-filtered product of the OH and TF coil

currents as is evident in Figure 3. The increased difficulty of accurately modeling the time-dependence of this intrinsic error field combined with the importance of general variations in plasma response motivated improvements in the active feedback correction of the OH×TF error field with a goal of minimizing or eliminating the need for PEFC term in the DEFC algorithm. In particular, measurements of the n=1 plasma response were improved through the optimal combination of both the upper and lower BP sensor arrays.

The methodology employed for improving n=1 mode detection was the identification of discharges with unstable and nearly pure n=1 RWMs which grow to amplitudes far above the background level and also saturate and persist at high amplitude for many growth times. Such discharges provide the most robust test of mode detection, since both fast (early growth) and slow (saturated state) mode dynamics must be tracked for mode detection to be successful. Figures 14a-b show the upper and lower BP signals for such a discharge. As seen in the figure, there is no detectable n=1 mode activity prior to 0.582s above the upper and lower n=1 offset amplitudes of 5 Gauss. After 0.586s there is a rapidly growing n=1 mode which reaches a maximum amplitude of 25-40 Gauss 2-3ms later. Thus, the peak amplitude normalized to the offset (i.e. an effective signal to noise ratio = SNR) is in the range of 5 to 8. The mode then decreases in amplitude and persists for at least another 10ms. One important observation is that the upper and lower array n=1 mode amplitudes can differ significantly - in this case the upper array measures an amplitude up to 1.6 times larger in peak amplitude and 2.5 times larger during the saturated phase. These differences between the upper and lower sensor responses add uncertainty in the mode identification when only one of the arrays is used for active feedback control of RFA.

At present these differences are unexplained, but may be a result of up/down

asymmetries in plasma shape. A simple average of the upper and lower sensor difference signals prior to toroidal Fourier decomposition into n=1 and 2 components is shown in Figure 14c. As shown in this figure, this averaging technique does substantially reduce the offset field to approximately 1 Gauss, but has the unphysical side-effect of decreasing the inferred n=1 mode amplitude to values 2 to 3 times lower than measured by the upper or lower arrays alone. Further, with this averaging technique, the inferred n=1 and n=2 amplitudes are comparable, and the n=1 mode rapid growth phase is delayed. Both of these results are inconsistent with the individual upper and lower array decompositions. From this averaging test, it is clear that simple upper-lower averaging of the BP array data is insufficient to capture the n=1 mode structure and growth.

To possibly improve the n=1 mode detection, the relative phase between the upper and lower BP arrays can be varied prior to averaging and Fourier decomposition. As described in more detail below, the toroidal phase-shift which provides the optimal discrimination between the n=1 and n=2-3 components is taken to be 150°. As shown in Figure 14d, with this toroidal phase shift between upper and lower arrays, the peak n=1 mode amplitude is 32 Gauss which is an intermediate value between the upper and lower array values, and the saturated value is approximately 1/2 of the peak value consistent with the average of the upper and lower array ratios. The offset field is also decreased to 4 Gauss with an SNR of 8 which matches the higher (and improved) SNR of the lower array. Importantly, with this toroidal phase shift $\Delta\Phi_{UL}$ of 150° and a Fourier decomposition into n=1-3 modes, the offset field is decreased to 3 Gauss and the SNR is increased to 10. Thus, by using optimal detection, the offset field is decreased by almost a factor of 2 and the SNR is doubled relative to the upper array commonly used for initial feedback control experiments (since the lower array had intermittent sensor

failures). Overall, this optimal averaging technique is less sensitive to the failure of an individual upper or lower sensor pair, since the Fourier singular value decomposition (SVD) into n=1-3 components is over-constrained by the use of both the upper and lower array data.

Since the optimal mode identification could be sensitive to details of the plasma equilibrium and mode growth characteristics, it is important to develop a robust mode detection technique that is relatively insensitive to $\Delta\Phi_{UL}$. The optimal range of $\Delta\Phi_{UL}$ must simultaneously provide a high n=1 mode amplitude representative of the individual arrays and provide a high ratio of n=1 to n=2 and 3 component amplitudes. Figure 15a shows the n=1-3 toroidal mode number decomposition for the mode field of Figure 14 averaged over the time range t=0.585 and 0.600s which includes both the mode growth and saturation phases. Figure 15b plots the ratio of the n=1 amplitude normalized to the square-root of the product of the n=2 and n=3 amplitudes. As seen in this figure, a high n=1 amplitude and high ratio of n=1 to n=2 and 3 components ($\geq$ that measured for $\Delta\Phi_{UL}$=0°) is achieved for relatively wide range of $\Delta\Phi_{UL}$=100-240°. The amplitude ratio peaks at 165° but is indeterminate at 180° (for equal weighting of upper and lower sensor signals). The choice of 150° was found to work as well or better than 165° for a range of outboard field-line pitch angle (safety factor) values, and also provides 2 times higher ratio of n=1 to n=2,3 amplitudes than at $\Delta\Phi_{UL}$=0° while also yielding n=1 mode amplitude comparable to the individual upper and lower arrays. Overall, the choice of $\Delta\Phi_{UL}$=150° provides two times higher discrimination of n=1 modes, doubles the SNR, and provides good mode identification for both fast-growing and saturated modes, all of which should enable the use of higher feedback gain for improved RFA and RWM suppression.

Utilizing the improved mode detection described above, experiments were

performed to optimize the feedback suppression of n=1 RFA. In particular, n=1 error-field pulses were purposely applied to plasmas operating with beta above the n=1 no-wall instability limit at times in the discharge with minimal intrinsic EF and with the RWM stabilized by rotation. The applied error field was sufficiently large that rotation damping from the EF slowed the plasma rotation, destabilized an n=1 RWM, and plasma disruption occurred. A comparison of the no applied EF (black) and applied EF (red) without feedback is shown in Figure 16. Then, n=1 active feedback control was applied, and the feedback phase and proportional gain were varied/scanned until the feedback system reduced all applied EF currents to nearly zero (i.e. eliminating the externally applied EF). At the optimal phase, the results of a gain scan are shown by the green and blue curves of Figure 16. As seen in Figure 16a, a proportional gain of $G_P = 0.7$ is sufficient to maintain high plasma beta by nearly nulling the applied n=1 current as shown in Figure 16b-c. In this way, a known n=1 error field was used to "train" the n=1 feedback control system to detect and suppress the plasma response to any n=1 error field. Then, the applied error field was removed and the n=1 feedback system left on to suppress RFA from any intrinsic EF. The improved mode detection was found to enable stable control at higher G_P=1-1.4, and G_P=2 was found to be marginally feedback unstable. Thus, improved n=1 mode detection not only enabled suppression of n=1 RFA by feedback alone, but also doubled the stable feedback gain. These improvements have also been useful for suppressing fast growing modes such as the RWM, and many n=1 RWM control experiments subsequently used the same gain and phase settings as used for RFA suppression.

2.3.2. $n > 1$ error field detection and correction The discovery of n=1 error fields in NSTX and the performance improvements from their correction motivated additional experiments investigating the possible importance of $n > 1$ error fields. In particular,

remaining asymmetries in the vertical field coil [10] were viewed as a potential source of n=2 or n=3 error field. Indeed, scans of the applied n=3 field amplitude and sign revealed important asymmetries in the plasma response to the applied field at high plasma beta. As shown in Figure 17a-c, I_P=900kA plasmas operating above the n=1 no-wall instability limit exhibited up to a factor of 2 change in pulse duration depending on the sign of a modest ($|B_R|$ = 4-6 Gauss at outboard mid-plane) externally applied n=3 error field. Experiments measuring the rotation near the q=2 and 3 surfaces (r/a = 0.6-0.7) showed that the rotation was maximized for negative RWM/EF coil 1 currents in the range of 200-300A, and that the rotation was 40-50% higher than for the opposite sign of n=3 coil current of the same magnitude. This result implies the existence of a fortuitous phase match between intrinsic n=3 EF and the n=3 field that the 6 coil RWM/EF coil system can apply. Further, the observed importance of rotation damping from intrinsic n=3 error fields is consistent with the previous usage of large externally applied n=3 error fields to reduce plasma rotation to the point where n=1 RWMs are destabilized [39].

In contrast, similar scans of the applied n=2 error field found little asymmetry in the plasma response, indicating that either n=2 intrinsic error fields are small in NSTX, or that the accessible toroidal phases of the n=2 correction field using a 6 coil system were not well matched to the toroidal phase of the intrinsic error field [43]. Measurements of the shape of the PF5 vertical field coils have been used to predict the intrinsic error fields from this coil as a function of toroidal mode number. Figure 18a shows that the PF5 coil (black) produces primarily n=3 error field and that the n=3 component (4 Gauss) is approximately 4 times larger than the next highest component which is the n=2 component (1 Gauss). Thus, the presence of the measured n=3 error field and lack of any significant n=2 error field is consistent with the shape measurements of

the PF5 coil. Further, for typical PF5 currents of -10kA, the required n=3 RWM/EF coil current to match the radial field amplitude of the PF5 coils is near 200A, which is consistent with the results shown in Figure 17. Further, Figure 18b shows that for positive I_{RWM1} coil current (and n=3) and negative PF5 coil current, the toroidal phase angle of the PF5 n=3 error field and the RWM/EF applied field are in good alignment and differ by only 20°. This implies that a negative I_{RWM1} is required for correction of an n=3 intrinsic error field from PF5, which is also consistent with Figure 17. Finally, because the RWM/EF coils are positioned very close to the PF5 coils on NSTX, the n=3 radial field profiles of the two coil systems should be very similar, and Figure 18c shows that this is indeed the case. Thus, the PF5 coil appears to a leading candidate for the source of the n=3 intrinsic error field in NSTX. Scans of the optimal error-field correction as a function of plasma current, toroidal field, and vertical field combined with quantitative comparisons between the predicted and measured toroidal flow damping have been performed to further improve understanding of non-resonant error fields in NSTX [43] with application to all tokamaks.

The above results imply that the ability to detect and correct n > 1 error fields is likely important for sustained operation above the n=1 no-wall stability limit when relying primarily on rotation for stabilization of the n=1 RWM. Such n > 1 error field correction is generally not accounted for in present tokamak devices including ITER. Expanding on the success of n=1 EFC, NSTX experiments have shown that simultaneous multiple-n EF correction can further improve plasma performance. By combining the optimized n=1 DEFC described in Section 2.3.1 with pre-programmed n=3 EF correction, record NSTX pulse-lengths of 1.3s were achieved at I_P=900kA. As shown in Figure 19a, and unlike previous operating scenarios in NSTX, the rotation at larger major radius ($R > 1.2m$) was observed to stay constant or increase even as

the central rotation decreased as the electron density increased throughout the shot to $f_{GW} > 0.75$. This rotation rise persists until a large ELM and a sustained H-mode to L-mode back-transition occurs at t=1.1s. As shown in Figure 19b, a period of high normalized beta = 5-5.5 and high toroidal beta = 15-18% free of low-frequency core MHD activity is sustained for 2 current redistribution times ($2\tau_{CR}$) and 15 energy confinement times ($15\tau_E$) using optimal error-field correction.

Starting from the conditions and mode control settings shown in Figure 19, the combination of optimized n=1 DEFC with pre-programmed n=3 EF correction was also readily extendible to a range of plasma currents I_P = 0.75-1.1MA typical of NSTX operation as illustrated in Figure 20a. In these discharges, the plasma beta was not disrupted by error-field induced rotation damping and the plasma duration was generally limited by loop voltage increases associated with confinement degradation from higher frequency MHD modes as q_{min} evolved toward 1, or by the current limit of the OH coil. As shown in Figure 20b, for all plasma currents tested, more than 90% of the available OH flux was consumed without major MHD events and low loop voltage was maintained until $I_{OH} \leq$-20kA where -24kA is the current limit of the OH transformer.

Further plasma improvements beyond sustained rotation and beta were achieved by optimizing the plasma current and heating power, and through coating the plasma facing components with evaporated lithium [44]. Figure 21a shows MHD spectrogram data from the longest discharge achieved to-date on NSTX, and as is evident from the figure, low-frequency MHD activity is completely avoided after t=0.5s. Figure 21b shows that the toroidal rotation is maintained at all radii measured - even near the plasma edge (R=1.4m). MSE-constrained reconstructions [41] and current profile analysis (not shown) indicate that the current profile reaches an equilibrium which is partially-inductively-driven (30-40%) and with q_{min} sustained near 1.2 (i.e. above 1 consistent

with the avoidance of low-n MHD). Figure 21c shows that the plasma current is sustained past the end of the TF flat-top, and Figure 21d shows that operation well above the approximate n=1 no-wall stability limit is sustained. Importantly, Figure 21e shows that the plasma toroidal beta sustained in this discharge is comparable to that expected to be used in an ST-based Component Test Facility (CTF) [45] designed to provide 1MW/m^2 neutron wall loading. The high toroidal beta is sustained for 3 current redistribution times, and is limited only by the OH and TF coil heating limits. These results represent a factor of 3-4 increase in duration of sustained beta above the n=1 no-wall limit relative to performance prior (shown in red) to improvements in plasma shaping [42] and error field correction and mode control, and a factor of 2 increase in duration above the no-wall limit relative to plasmas including improved shaping but without error field correction and mode control [41, 42]. Thus, control of the resonant field amplification and resistive wall modes is a very important tool for performance optimization in NSTX as previously observed in high-beta conventional aspect ratio tokamaks [46, 47].

2.4. Comparison of RWM critical rotation data to theory

As is evident from the results described in Section 2.3, it is generally desirable to operate in a regime where the toroidal rotation is sufficiently high to stabilize the n=1 RWM thereby enabling relatively slow feedback-control of n=1 RFA to maintain the toroidal rotation. In general, intrinsic error fields and any error-field correction coils will have different field spectra in the plasma region. While minimization of the resonant components of the total field can largely eliminate locked modes at low to moderate β, at higher β the amplification of non-resonant components can also lead to toroidal flow damping and RWM destabilization. The question then becomes where in the plasma (i.e. at which q surfaces) is it most important to maintain the rotation to maintain

RWM stability.

The n=3 EFC experiments described in Section 2.3.2 shed significant light on this question. The RWM critical rotation results obtained here utilize n=3 magnetic braking to vary the plasma rotation and induce n=1 RWM instabilities but with smaller n=3 field amplitudes than typically used to study NTV flow damping [9] and RWM stability [39]. The usage of n=1 magnetic braking to study the n=1 RWM [48, 49] has previously been shown to lead to critical rotation results that differ from those obtained with a combination of balanced neutral beam injection and reduced n=1 magnetic braking from optimized n=1 error field correction [49]. The results obtained here utilize a braking field with toroidal mode number n=3 which is not resonant with the n=1 RWM under study. This technique substantially reduces the uncertainty in determining the critical rotation value and in ascertaining the dominant physics in RWM stabilization. Importantly, for n=3 EFC it is observed that the edge rotation for $\rho = r/a > 0.7$ largely determines the stability of these discharges and the resultant pulse-length in NSTX. Further, by varying the degree of n=3 EFC it is possible to bracket the critical rotation frequency for the n=1 RWM between stable and unstable values.

Figure 22 shows a comparison of the rotation profiles of two nearly identical plasmas differing only by the absence (124427) or presence (124428) of n=3 EFC. In the absence of n=3 EFC, n=1 magnetic sensor measurements indicate the n=1 RWM becomes unstable near t=0.580s and grows until t=0.62s after which the plasma undergoes a beta collapse and eventual plasma current disruption. Thus, the red curves in Figure 22 are representative of n=1 RWM marginal stability. With n=3 EFC, the plasma exhibits no n=1 RWM instability during the same period, and the plasma current flat-top lasts until t=1.2s. As shown in Figure 22, during optimal n=3 EFC, the core rotation actually slightly decreases by 10%, whereas the rotation for normalized minor radii $\rho > 0.7$

increased by 50-100%. In terms of the corresponding q profile during optimal n=3 EFC, the rotation changes little near the $q = 2$ surface, but increases substantially for $q \geq 3$ in the plasma edge region. Thus, for these discharges, the n=1 RWM stability appears to be most strongly influenced by stabilization physics in the plasma edge region rather than the plasma core, and the surfaces with $q = 3 - 6$ may be particularly important since they tend to have the lowest toroidal rotation even with EFC applied.

For RWM stability, the plasma angular toroidal rotation frequency Ω_ϕ is commonly normalized to the inverse Alfven time $\tau_{Alfven} \equiv R_0/v_A(0)$ [50] where R_0 is the major radius of the plasma geometric center and v_A is the Alfven velocity computed at the plasma magnetic axis. For the plasmas in Figure 22, the normalized rotation frequency $\Omega_\phi \tau_A$ is relatively high $\approx 18\%$ in the plasma core, whereas $\Omega_\phi \tau_A$ is significantly lower outside the core = 5%, 0.8-2%, 0.3-0.8% at the q=2, 3, and 4 surfaces respectively. Similar n=1 RWM critical rotation values $\Omega_\phi \tau_A$ values = 0.3-1% (in the counter direction) near the $q = 3$ and 4 surfaces are also evident in published DIII-D data in plasmas with low rotation near the $q = 2$ surface using balanced NBI [51] and when n=1 magnetic braking results are compared to balanced beam results [49]. Thus, the rotation in the plasma near-edge region may be an important factor in determining RWM stability in both NSTX and DIII-D plasmas.

The results above motivate comparisons between the observed and predicted RWM critical rotation. A leading simulation tool for RWM stability calculations code is the MARS code [52, 53] based on parallel sound-wave damping extended to include drift-kinetic damping in the high-aspect-ratio circular limit (MARS-F) [54] and a more recent fully toroidal self-consistent drift-kinetic model (MARS-K) [55]. None of the MARS damping models described here include the effects of fast particles, energy-dependent collisionality, or poloidal rotation.

The collisionless dissipation model describing the RWM stabilization involves resonant mode-particle interactions including passing and trapped particle transit and bounce motion, orbit precession, diamagnetic drift, and $\vec{E} \times \vec{B}$ rotation [56, 55]. The theory is most tractable in the limit where precession and diamagnetic drift frequencies are sub-dominant to the $\vec{E} \times \vec{B}$ frequency $\omega_E \equiv -d\Phi_0/d\psi$ where Φ_0 is the electrostatic potential and ψ is the poloidal flux function. Further simplification is afforded by a high-aspect-ratio circular plasma approximation which specifies the poloidal dependence of the magnetic field strength on a flux surface as

$$B = B_0(1 - \epsilon_r \cos\theta) \tag{5}$$

when computing the passing and trapped particle orbit times. Here B_0 and ϵ_r are the average magnetic field strength and inverse aspect ratio on a flux surface respectively.

In this limit, the dissipation from trapped and circulating particles can be computed nearly completely analytically. For example, the dissipation from circulating particles [54] is proportional to:

$$D_C(\Omega_C, \epsilon_r) = \frac{\sqrt{\pi}}{2}\Omega_C^7 \int_0^{1/(1+\epsilon_r)} \tau^8 \exp(-\tau^2\Omega_C^2)(2-\lambda)^2 d\lambda \tag{6}$$

where τ is a normalized orbit time, $\lambda = \mu B_0/E$, $\Omega_C \equiv \omega/|nq - m'|\omega_s$, the sound frequency $\omega_s \equiv (2T/M)^{1/2}/qR$, and ω is the relative frequency between the propagating RWM and ω_E which is approximately ω_E since the RWM generally propagates slowly in the lab frame. The dissipation from trapped particles scales similarly, and also has a very strong frequency dependence $\propto \omega^7\tau^8$. From this scaling it is apparent that at fixed dissipation, the critical rotation frequency for RWM stability should scale as ω_s. Interestingly, such a normalization of the critical rotation frequency to the sound frequency does appear to be a more aspect-ratio-invariant representation of the critical rotation when NSTX RWM data is compared to DIII-D as shown in Figures 15 and 16 of Reference [50]. However, this comparison must be treated with some caution since

the rotation at a single resonant surface is generally not a good metric of the RWM critical rotation due to the distributed nature of the dissipation. Further, there is also the possibility that $n = 1$ magnetic braking in the DIII-D experiments of Reference [50] increases the inferred critical rotation [49]. Finally, accurate and local calculations of the particle orbit times and sound-wave frequencies in the region of maximum dissipation would also clearly be needed for such a comparison given the strong predicted τ^8 scaling of the dissipation in Equation 6.

Since the particle orbit times are determined to a large extent by the mirror-ratio on a flux surface and are largest at the trapped-passing boundary, it is important to utilize the actual values of $|B|$ on a flux surface. By defining $B_0 = (B_{max} + B_{min})/2$ and an effective inverse aspect ratio $\epsilon_B = (B_{max} - B_{min})/2$ and replacing ϵ_r with ϵ_B in Equation 5, the trapped-passing boundary and orbit times can be much more accurately calculated. At high aspect ratio and for circular cross-section, the "global" estimate of the effective local inverse aspect ratio $= \epsilon_g \equiv a/R_0\rho_{pol}$ used in the MARS-F semi-kinetic model is approximately equal to ϵ_B. However, for the NSTX plasmas studied here with low aspect ratio and core safety factor near 1, ϵ_B can deviate significantly from ϵ_g. In particular, $\epsilon_B \approx 0.65\epsilon_g$ for ρ_{pol} values with $q \leq 5$ and $\epsilon_B \approx 0.8\epsilon_g$ near the plasma edge.

Beyond the change in effective inverse aspect ratio, general geometry effects such as flux-surface shaping (ellipticity, triangularity) also modify the orbit time. It is generally found that by utilizing ϵ_B in Equation 5 not only is the trapped-passing boundary accurately identified, but the analytically computed orbit times are in reasonable agreement with orbit times computed with numerical integration in general tokamak geometry even in the core of low-aspect-ratio NSTX plasmas. However, at larger minor radii in NSTX plasmas, the analytic formulae for orbit times can deviate significantly from the numerically computed values including the full plasma geometry even when ϵ_B

is used for the effective inverse aspect ratio.

Investigations of the dependence of the orbit times on plasma geometry have shown that relatively simple extensions of the analytic expressions can capture the most important features of the full geometry calculations. The extended formulae for the normalized (dimensionless) transit and bounce orbit times τ are:

$$\begin{aligned} \tau &= \frac{v}{Rq\omega_{transit}} = \frac{2}{\pi}\frac{(c_0 + c_1\lambda + c_2 K(k))k}{\sqrt{2\lambda\epsilon_B}} \qquad k^2 = \frac{2\lambda\epsilon_B}{1-\lambda(1-\epsilon_B)} \\ \tau &= \frac{v}{Rq\omega_{bounce}} = \frac{2}{\pi}\frac{(c_0 + c_1\lambda + c_2 K(k))}{\sqrt{2\lambda\epsilon_B}} \qquad k^2 = \frac{1-\lambda(1-\epsilon_B)}{2\lambda\epsilon_B} \end{aligned} \tag{7}$$

where the particle velocity $v = \sqrt{2E/M}$, $K(k)$ is the complete elliptic integral of the first kind, and R and q are the geometric center and safety factor of the flux surface in question. The coefficients c_0, c_1, c_2 depend on the flux-surface shape and are strongly influenced by the presence of the field-null near the boundary of diverted plasmas. Thus, analytic expressions for the coefficients are difficult to derive in general, and are instead determined by least-squares fitting to numerical orbit time weighted to fit the region near the trapped-passing boundary. In the high-aspect-ratio circular plasma limit $c_0 = c_1 = 0$ and $c_2 = 1$.

Figure 23 plots the trapped and passing particle orbit times $\tau_{orbit} = 2\pi/\omega_{orbit}$ multiplied by the particle velocity in the outer half of the plasma minor radius $\rho_{pol} \equiv \sqrt{\hat{\psi}_{pol}} = 0.5$, 0.7, and 0.9 for the RWM-unstable plasma shown in Figure 22. As is evident from Figure 23, the high-A circular plasma orbit time using ϵ_g (red) as used in the MARS-F code does not match the trapped-passing boundary well, nor does it match the magnitude of the general geometry (numerically integrated) orbit time (black). As is also evident from the figure, the same formulation using ϵ_B (blue) matches the trapped-passing boundary well and improves the agreement between the analytic and general geometry orbit time. Further, the improved generalized analytic model (green) using the formulation in Equations 7 fits the full general geometry orbit time (black)

well near the trapped-passing boundary and for most pitch-angles, but can deviate from the general geometry value for deeply-trapped particles due to the contribution of the poloidal magnetic field on $|B|$ and because of plasma elongation. As seen in this figure, relative to the orbit time computed via numerical integration, the high-A circular analytic approximation (blue) using ϵ_B (Equation 7 with $c_0 = c_1 = 0, c_2 = 1$) under-predicts the orbit time by 25% near the half-radius and over-predicts it by 40-50% near the plasma edge. Thus, depending on the dominant spatial location of the dissipation, the general-geometry orbit-time calculations could lead to either increased or decreased dissipation. However, the semi-kinetic damping model in MARS-F uses ϵ_g instead of ϵ_B which, as is evident from Equation 7, tends to decrease the orbit times nearly everywhere since $\epsilon_g > \epsilon_B$ in NSTX. Thus, the overall effect of the general geometry corrections to the orbit times for NSTX in MARS-F is to increase the orbit times over much of the plasma minor radius, which from Equation 6 is expected to increase the dissipation and reduce the predicted critical rotation.

Figure 24a plots a comparison of the MARS-F semi-kinetic damping model predictions of the RWM growth rate using the high-A circular cross-section approximation for the particle orbit times (red) and the general-geometry analytic fit to the particle orbit times (blue) for the RWM-unstable discharge 124427 at t=0.575s just prior to RWM onset. The rotation profile used in the calculations = Ω_ϕ is the carbon impurity toroidal rotation profile and is linearly scaled from the experimental rotation profile = $\Omega_{\phi-expt}$. Both growth rate curves show a non-monotonic dependence on plasma rotation frequency from the safety factor and orbit-time dependence of the dissipation models. Further, both models indicate the presence of several "roots" which individually become stabilized at sufficiently high rotation. The presence of multiple roots is most apparent for the general-geometry analytic fit case in which two growth-

rate curves intersect near $\Omega_\phi/\Omega_{\phi-expt} = 0.15$. Numerically, all roots with positive growth-rate obtained at low rotation have thus far been found to be stabilized at sufficiently high rotation. Consistent with the expectations discussed above, the predicted critical rotation using general-geometry orbit times is lower than for high-A circular cross-section orbit times. As is evident from this figure, the MARS-F calculations predict critical rotation 2.5 to 4 times lower than experimentally observed.

The sound-wave damping model [52, 53] is another commonly used model based on parallel ion Landau damping and ignoring toroidal trapping effects. Figure 24b plots predictions of the RWM growth rate for different Landau damping multipliers $\kappa_{||}$ where $\kappa_{||} = 0.5$ corresponds to the cylindrical (zero particle trapping) limit. As shown in the figure, in the weak dissipation limit ($\kappa_{||} = 0.049$) the critical rotation frequency is 2.5 times lower than experimentally observed, and in the strong dissipation limit ($\kappa_{||} = 0.5$) the critical rotation frequency is 4 times lower than experimentally observed. Thus, both the semi-kinetic and sound-wave damping models substantially under-predict the measured n=1 RWM critical rotation in NSTX plasmas. Significant discrepancies between the measured and predicted critical rotation using these models has also been observed in DIII-D [57]. These results suggest that different or extended damping models with reduced dissipation are needed to explain the NSTX data.

One potentially important contribution to the RWM mode damping physics is the effect of plasma collisionality. Collisionality can enter either through the plasma resistivity η (generally destabilizing) or through the mode dissipation directly. Non-zero resistivity can lead to tearing instability if the rotation is low and therefore the dissipation is weak, and studies of the unstable RWM growth rate varying the resistivity for NSTX (using MARS-F) do indeed observe an $\gamma \propto \eta^{\frac{3}{5}}$ dependence consistent with tearing theory in the constant ψ approximation [58]. However, at sufficiently

high rotation, dissipation dominates and the critical rotation changes very little with resistivity for the experimental resistivity values. This result is evident by comparing the blue curve in Figure 25a which shows a marginal normalized rotation of 0.26 including the experimental parallel resistivity profile versus 0.24 with zero resistivity shown by the blue curve in Figure 24a. While the critical rotation is not strongly increased by resistivity, the mode growth rate for rotation below marginal stability is increased by 20% at normalized rotation $\Omega_\phi/\Omega_{\phi-expt}$ =0.05 and by a factor of 2 at $\Omega_\phi/\Omega_{\phi-expt}$ = 0.2. Figure 25a also shows that the strongest dissipation (lowest growth rate) comes from the circulating particles, but both the circulating and trapped particles yield similar marginal stability thresholds, presumably due to the strong dependence of the dissipation on orbit time as described above. Ion collisionality is another potentially important effect, and Figure 24b shows the profile of the ion collision frequency normalized to the thermal ion bounce time ν_i^* [59]. As seen in the figure, near the plasma edge for surfaces with $q \geq 4$, the normalized ion collisionality is near unity. Thus, ion collisions could potentially induce wave-particle decorrelation during the particle orbit and reduce the dissipation.

Additional factors that are potentially important in RWM stability predictions include an accurate determination of the plasma $E \times B$ drift frequency ω_E and the inclusion of the real part of the mode eigen-frequency ω_r in the dispersion relation.

Because the differences between the toroidal rotation frequencies of different ion species may be non-negligible, the species index "C" is applied to the carbon impurity rotation frequencies that follow. Further, because of the low toroidal rotation frequency $\Omega_{\phi-C}$ of the carbon impurities, calculations of ω_E should also include the contributions of the carbon impurity pressure gradient (diamagnetic flow) and poloidal flow. Poloidal flow measurements are not yet available for the plasmas treated here, but the ion

diamagnetic data is available and substantially changes the computed ω_E profiles outside the q = 2 surface. As shown in Figure 26a, the inclusion of the carbon diamagnetic contribution reduces ω_E by 25% near the q=2 surface, changes the sign of the rotation near q=3, and reduces the rotation by up to a factor of 2 at the plasma edge. In this figure, the unmodified rotation profile ($\omega_E = \Omega_{\phi-C}$) is shown in black and the experimental profile ($\omega_E = \Omega_{\phi-C} - \omega_{*C}$) is shown in green. Several nearby rotation profiles with scaled ω_{*C} values are also shown (red and blue) and are included to test the sensitivity of the predicted stability to small deviations of the rotation profile relative to the experimental value. Figure 26b shows the important effect of including ω_{*C} in ω_E, namely the doubling of the normalized predicted critical rotation frequency ω_E/ω_{E-expt} from 0.25-0.3 to 0.5-0.6. The mode ω_r has also been included in the calculations of Figure 26b and increases ω_E/ω_{E-expt} by only 0.02 to 0.05. Thus, the inclusion of ω_{*C} in ω_E is responsible for nearly all of the increase in the predicted critical rotation. These results indicate that details of the edge rotation profile and resultant resonances are very important for predicting the marginal stability of the n=1 RWM.

Recently, more comprehensive dissipation models [56, 55, 60] including the effects of collisions (using simplified collision operators) and other kinetic effects have been implemented in the MISK code [56] and applied to dedicated RWM critical rotation experiments [61, 62]. In these experiments, the near-edge carbon rotation frequency is also observed to tend to 1-2kHz at RWM marginal stability. For such plasmas, the effects of collisions are not computed to be dominant for NSTX parameters, but at high collisionality the critical rotation at low rotation can be increased. One important finding using the MISK code is that RWM stabilization can sometimes be reduced to near marginality if the $E \times B$ rotation is intermediate between the precession and bounce frequencies [61, 62]. Such a condition can occur for rotation values near the measured

critical rotation in the error-field correction studies discussed above and may explain the RWM stability behavior observed during n=3 EFC. A key question is the generality and robustness of this result at intermediate (near the experimental) rotation values. If energetic particles are found to be important for the RWM in future MISK or MARS-K calculations, such effects could also modify the interpretation of RWM stability described here.

3. Summary

Systematic studies of the detection and correction of low-n magnetic error fields have been performed in the low-aspect-ratio NSTX device for the first time. Error fields with n=1 have been detected which result from small motion of the toroidal field coil resulting from an electromagnetic interaction between the toroidal field and ohmic heating coil. A detailed time-dependent model of this n=1 error field has been developed to enable EF correction and lock-mode experiments. Using the n=1 EF model to account for intrinsic n=1 error fields, the measured threshold for the onset of n=1 locked modes shows a linear scaling with plasma density, a weak to near inverse dependence on toroidal field, and a positive scaling with local magnetic shear. These results appear to extrapolate to a favorable error field threshold for ITER. Perturbed equilibrium calculations find that the plasma response must be included to explain the empirically determined optimal correction of NSTX n=1 error fields and these calculations also indicate that local magnetic shear may play an important role in the locking physics. In high-beta NSTX plasmas exceeding the n=1 no-wall stability limit, the RWM can be stabilized by plasma rotation provided there is sufficient active suppression of n=1 amplified error fields which otherwise slow the plasma rotation. Robust detection and suppression of n=1 RFA and RWMs has been achieved using an extensive array of non-axisymmetric poloidal

field sensors optimized to detect n=1 field perturbations with maximum signal-to-noise. Higher-n (n=3) error fields have been discovered, and the correction of these error fields has led to sustained high rotation and record durations free of low-frequency core MHD activity. During n=3 error field correction, the measured critical rotation for the n=1 RWM is a factor of 1.6 to 2 times higher than predicted by the MARS-F code using the semi-kinetic damping model which includes wave-particle resonances between the $E \times B$ rotation and trapped and passing orbit motion. The measured and predicted critical rotation frequency is quite sensitive to the detailed structure of the $E \times B$ rotation profile near the plasma edge, and future work will focus on further understanding this sensitivity. MISK analysis of similar NSTX plasmas including a fuller range of kinetic effects finds that instability may be possible for intermediate rotation frequencies near the experimental value and is an additional topic for future research.

Acknowledgments

The authors wish to thank H. Kugel, R. Kaita, and other members of the NSTX team who assisted in the application of in-vessel lithium coatings which contributed to the achievement of MHD-free long-pulse plasmas. Special thanks also to D. Mastrovito and C.A. Ludescher-Furth for implementing the real-time mode identification and active feedback control algorithms. This work was supported by the United States Department of Energy under contract numbers DE-AC02-09CH11466 (PPPL) and DE-AC05-00OR22725 (ORNL) and grant number DE-FG02-99ER54524 (Columbia University).

References

[1] SAIBENE, G., OYAMA, N., LNNROTH, J., ANDREW, Y., de la Luna, E., et al., Nucl. Fus. **47** (2007) 969.

[2] La Haye, R. J., FITZPATRICK, R., HENDER, T. C., MORRIS, A. W., SCOVILLE, J. T., et al., Phys. Fluids B **4** (1992) 2098.

[3] BUTTERY, R. J., DE'BENEDETTI, M., HENDER, T. C., and TUBBING, B. J. D., Nucl. Fus. **40** (2000) 807.

[4] LAZZARO, E., BUTTERY, R. J., HENDER, T. C., ZANCA, P., FITZPATRICK, R., et al., Phys. Plasmas **9** (2002) 3906.

[5] SCOVILLE, J. T. and La Haye, R. J., Nucl. Fus. **43** (2003) 250.

[6] WOLFE, S. M., HUTCHINSON, I. H., GRANETZ, R. S., RICE, J., HUBBARD, A., et al., Phys. Plasmas **12** (2005) 056110.

[7] BOOZER, A. H., Phys. Plasmas **10** (2003) 1458.

[8] SHAING, K. C., HIRSHMAN, S. P., and CALLEN, J. D., Phys. Fluids **29** (1986) 521.

[9] ZHU, W., SABBAGH, S. A., BELL, R. E., BIALEK, J. M., BELL, M. G., et al., Phys. Rev. Lett. **96** (2006) 225002.

[10] MENARD, J. E., BELL, M. G., BELL, R. E., FREDRICKSON, E. D., GATES, D. A., et al., Nucl. Fus. **43** (2003) 330.

[11] HENDER, T. C., FITZPATRICK, R., MORRIS, A. W., CAROLAN, P. G., DURST, R. D., et al., Nucl. Fus. **32** (1992) 2091.

[12] FITZPATRICK, R., Nucl. Fus. **33** (1993) 1049.

[13] TAKAMURA, S., KIKUCHI, Y., UESUGI, Y., and KOBAYASHI, M., Nucl. Fus. **43** (2003) 393.

[14] COLE, A. and FITZPATRICK, R., Phys. Plasmas **13** (2006) 032503.

[15] KIKUCHI, Y., DE BOCK, M. F. M., FINKEN, K. H., JAKUBOWSKI, M., JASPERS, R., et al., Phys. Rev. Lett. **97** (2006) 085003.

[16] MILITELLO, F. and WAELBROECK, F. L., Nucl. Fus. **49** (2009) 065018.

[17] KOSLOWSKI, H. R., WESTERHOF, E., DE BOCK, M., CLASSEN, I., JASPERS, R., et al., Plasma Phys. and Contr. Fus. **48** (2006) B53.

[18] COLE, A. J., HEGNA, C. C., and CALLEN, J. D., Phys. Rev. Lett. **99** (2007) 065001.

[19] COLE, A. J., HEGNA, C. C., and CALLEN, J. D., Phys. Plasmas **15** (2008) 056102.

[20] HOWELL, D. F., HENDER, T. C., and CUNNINGHAM, G., Nucl. Fus. **47** (2007) 1336.

[21] MENARD, J. E., BELL, M. G., BELL, R. E., GATES, D. A., KAYE, S. M., et al., Phys. Plasmas **11** (2004) 639.

[22] PARK, J.-K., BOOZER, A. H., and GLASSER, A. H., Phys. Plasmas **14** (2007) 052110.

[23] PARK, J.-K., BOOZER, A., and MENARD, J. E., Phys. Plasmas **15** (2008).

[24] MENARD, J. E., BELL, R. E., FREDRICKSON, E. D., GATES, D. A., KAYE, S. M., et al., Nucl. Fus. **45** (2005) 539.

[25] BUTTERY, R. J., De' Benedetti, M., GATES, D. A., GRIBOV, Y., HENDER, T. C., et al., Nucl. Fus. **39** (1999) 1827.

[26] PARK, J.-K., SCHAFFER, M. J., MENARD, J. E., and BOOZER, A. H., Phys. Rev. Lett. **99** (2007) 195003.

[27] CONNOR, J. W. and TAYLOR, J. B., Nucl. Fus. **17** (1977) 1047.

[28] CONNOR, J. W., Plasma Phys. and Contr. Fus. **30** (1988) 619.

[29] AMOSKOV, V., BELOV, A., BELYAKOV, V., FILATOV, O., GRIBOV, Y., et al., Plasma Devices and Operations **13** (2005) 87.

[30] PARK, J.-K., BOOZER, A. H., MENARD, J. E., and SCHAFFER, M. J., Nucl. Fus. **48** (2008) 045006.

[31] GREENWALD, M., TERRY, J. L., WOLFE, S. M., EJIMA, S., BELL, M. G., et al., Nucl. Fus. **28** (1988) 2199.

[32] GREENWALD, M., Plasma Phys. and Contr. Fus. **44** (2002) R27.

[33] WILSON, J. R., BELL, R. E., BERNABEI, S., BITTER, M., BONOLI, P., et al., Phys. Plasmas **10** (2003) 1733.

[34] SABBAGH, S. A., BIALEK, J. M., BELL, R. E., GLASSER, A. H., LEBLANC, B. P., et al., Nucl. Fus. **44** (2004) 560.

[35] SONTAG, A. C., SABBAGH, S. A., ZHU, W., BIALEK, J. M., MENARD, J. E., et al., Phys. Plasmas **12** (2005) 056112.

[36] BELL, R. E., Rev. Sci. Instrum. **77** (2006) 10E902.

[37] MENARD, J. E., BELL, M. G., BELL, R. E., BERNABEI, S., BIALEK, J., et al., Nucl. Fus. **47** (2007) S645.

[38] GATES, D. A., FERRON, J. R., BELL, M., GIBNEY, T., JOHNSON, R., et al., Nucl. Fus. **46** (2006) 17.

[39] SABBAGH, S. A., BELL, R. E., MENARD, J. E., GATES, D. A., SONTAG, A. C., et al., Phys. Rev. Lett. **97** (2006) 045004.

[40] GERHARDT, S. P., BRENNAN, D. P., BUTTERY, R., LA HAYE, R. J., SABBAGH, S., et al., Nucl. Fus. **49** (2009) 032003.

[41] MENARD, J. E., BELL, R. E., GATES, D. A., KAYE, S. M., LEBLANC, B. P., et al., Phys. Rev. Lett. **97** (2006) 095002.

[42] GATES, D. A., MAINGI, R., MENARD, J., KAYE, S., SABBAGH, S. A., et al., Phys. Plasmas **13** (2006) 056122.

[43] GERHARDT, S. P., MENARD, J. E., PARK, J.-K., BELL, R., GATES, D. A., et al., Observation and correction of non-resonant error fields in NSTX, 2009, submitted to Plasma Physics and Controlled Fusion.

[44] KUGEL, H. W., MANSFIELD, D., MAINGI, R., BELL, M. G., BELL, R. E., et al., J. Nucl. Mater. **390-391** (2009) 1000.

[45] PENG, Y.-K. M., FOGARTY, P. J., BURGESS, T. W., STRICKLER, D. J., NELSON, B. E., et al., Plasma Phys. and Contr. Fus. **47** (2005) B263.

[46] GAROFALO, A. M., STRAIT, E. J., JOHNSON, L. C., LA HAYE, R. J., LAZARUS, E. A., et al., Phys. Rev. Lett. **89** (2002) 235001.

[47] STRAIT, E. J., BIALEK, J., BOGATU, N., CHANCE, M., CHU, M. S., et al., Nucl. Fus. **43** (2003) 430.

[48] LA HAYE, R. J., BONDESON, A., CHU, M. S., GAROFALO, A. M., LIU, Y.-Q., et al., Nucl. Fus. **44** (2004) 1197.

[49] REIMERDES, H., GAROFALO, A. M., JACKSON, G. L., OKABAYASHI, M., STRAIT, E. J., et al., Phys. Rev. Lett. **98** (2007) 055001.

[50] REIMERDES, H., HENDER, T. C., SABBAGH, S. A., BIALEK, J. M., CHU, M. S., et al., Phys. Plasmas **13** (2006) 056107.

[51] STRAIT, E. J., GAROFALO, A. M., JACKSON, G. L., OKABAYASHI, M., REIMERDES, H., et al., Phys. Plasmas **14** (2007) 056101.

[52] BONDESON, A. and WARD, D. J., Phys. Rev. Lett. **72** (1994) 2709.

[53] CHU, M. S., GREENE, J. M., JENSEN, T. H., MILLER, R. L., BONDESON, A., et al., Phys. Plasmas **2** (1995) 2236.

[54] BONDESON, A. and CHU, M. S., Phys. Plasmas **3** (1996) 3013.

[55] LIU, Y. Q., CHU, M. S., GIMBLETT, C. G., and HASTIE, R. J., Phys. Plasmas (2008) 092505.

[56] HU, B., BETTI, R., and MANICKAM, J., Phys. Plasmas **12** (2005) 057301.

[57] REIMERDES, H., GAROFALO, A. M., OKABAYASHI, M., STRAIT, E. J., BETTI, R., et al., Plasma Phys. and Contr. Fus. **49** (2007) B349.

[58] FURTH, H. P., RUTHERFORD, P. H., and SELBERG, H., Phys. Fluids **16** (1973) 1054.

[59] SAUTER, O., ANGIONI, C., and LIN-LIU, Y. R., Phys. Plasmas **6** (1999) 2834.

[60] LIU, Y., CHU, M. S., CHAPMAN, I. T., and HENDER, T. C., Phys. Plasmas **15** (2008) 112503.

[61] SABBAGH, S. A., BERKERY, J. W., BELL, R. E., BIALEK, J. M., GERHARDT, S. P., et al., Nucl. Fus. **50** (2010) 025020.

[62] BERKERY, J. W., SABBAGH, S. A., BETTI, R., HU, B., BELL, R. E., et al., Phys. Rev. Lett. **104** (2010) 035003.

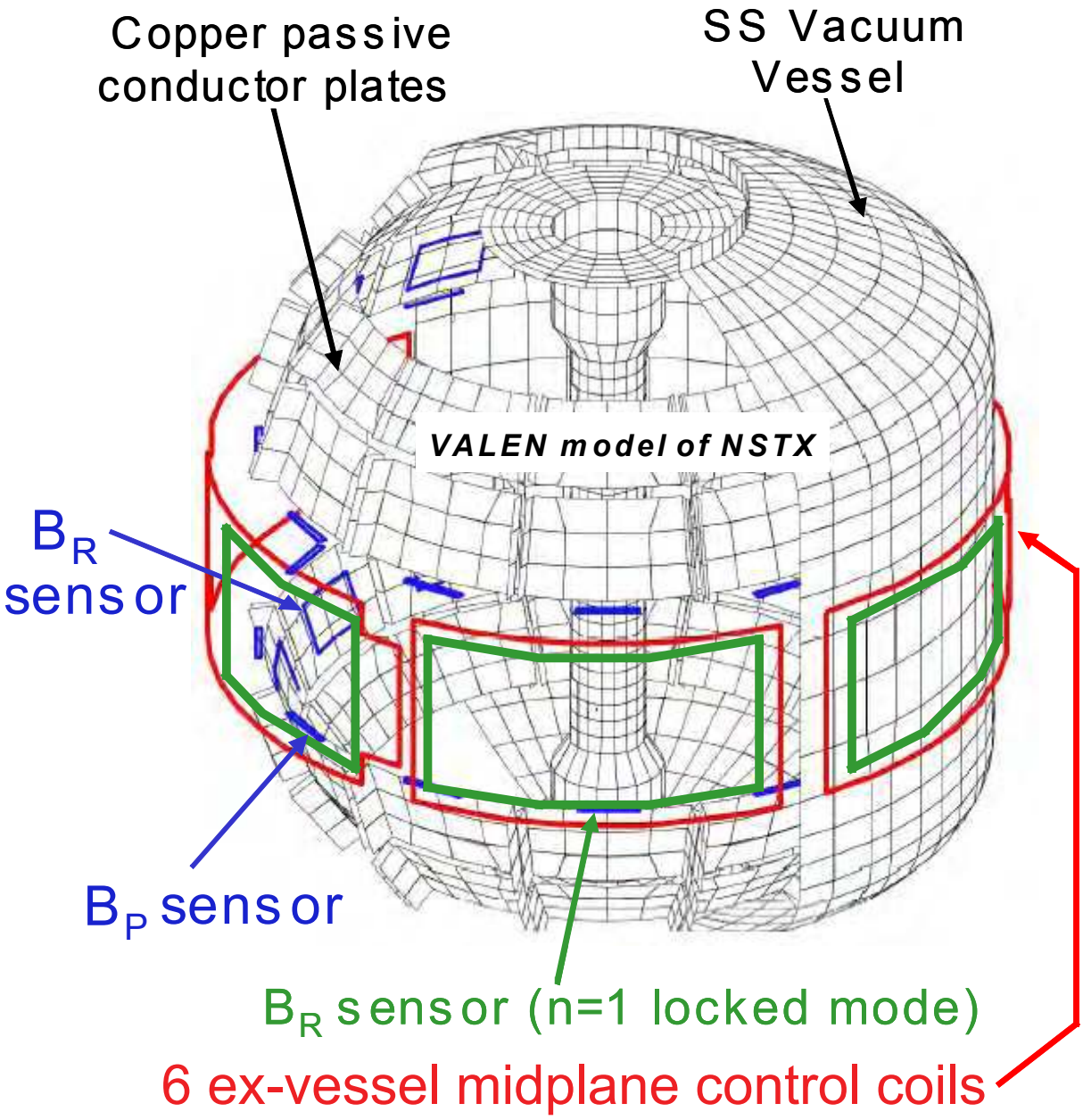

Figure 1. VALEN model of NSTX conducting structure showing vacuum vessel and passive plates. In-vessel radial (BR) and poloidal (BP) magnetic field sensors are shown in blue, ex-vessel n=1 locked-mode sensors are shown in green, and 6 ex-vessel resistive wall mode/error field (RWM/EF) control coils are shown in red.

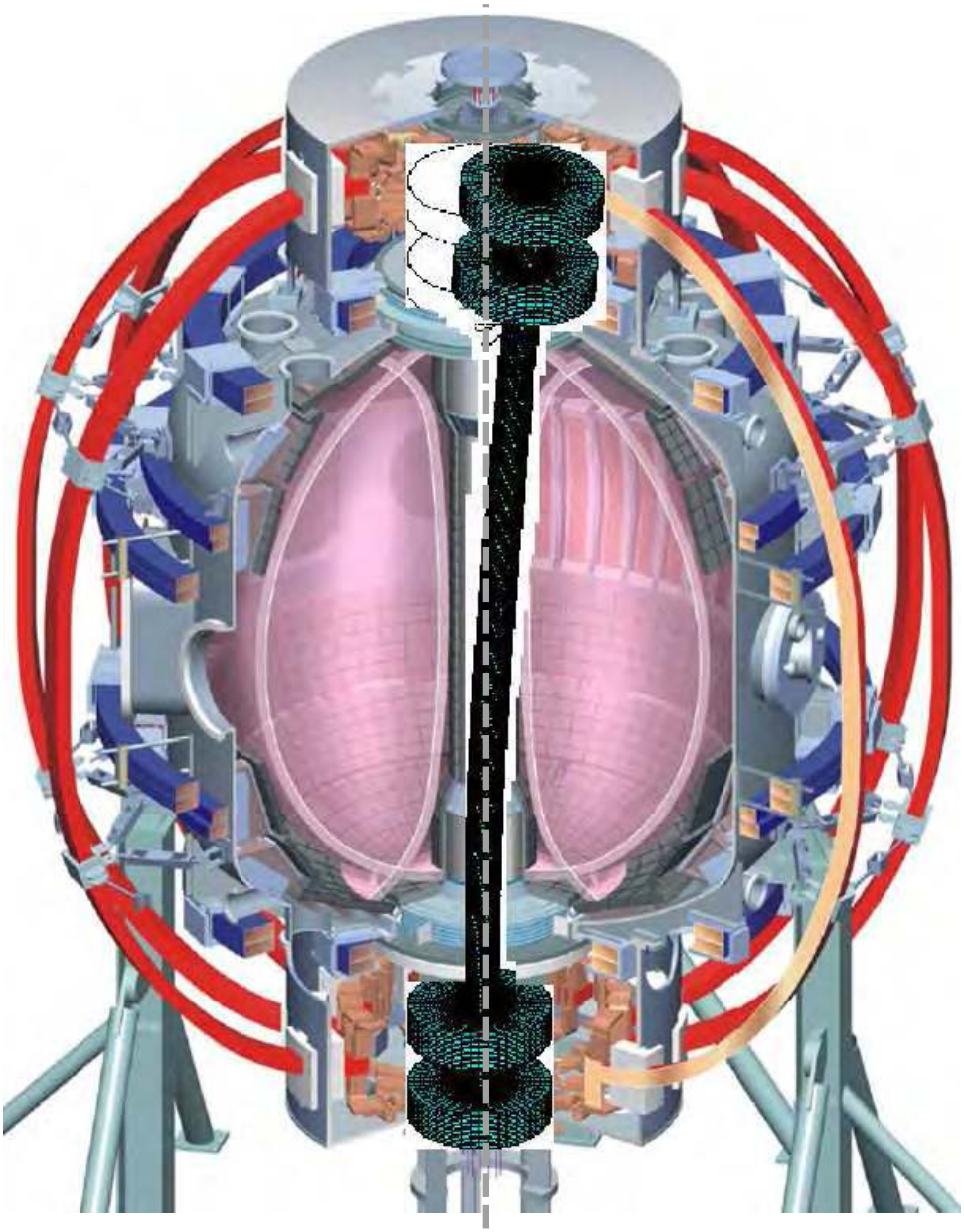

Figure 2. Illustration of motion of toroidal field (TF) coil central rod (black vertical cylinder) relative to poloidal field (PF) coils (blue) and TF coil outer return windings (red). The TF coil motion is predominantly tilt with the bottom of the coil approximately fixed. The motion of the TF has been exaggerated above to illustrate the direction of motion.

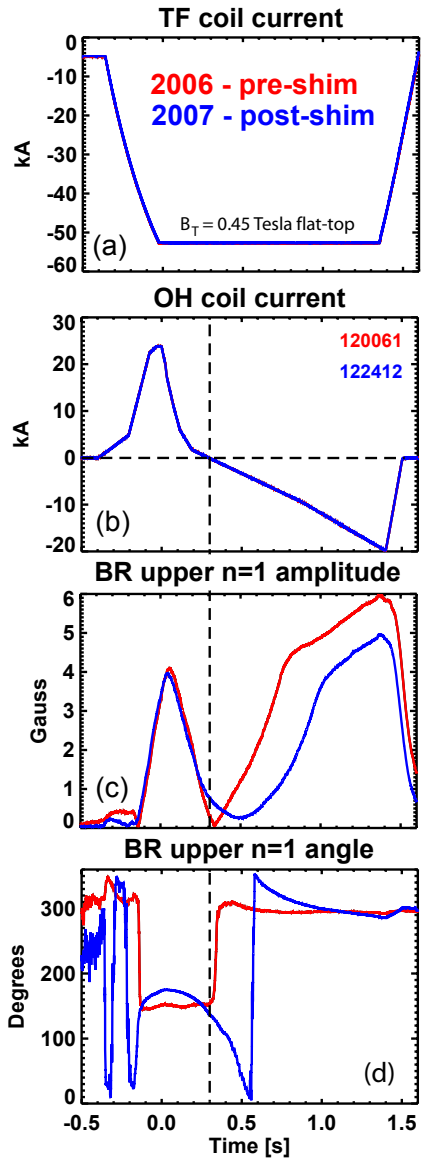

Figure 3. (a) Toroidal field (TF) and (b) ohmic heating (OH) coil current versus time before (red) and after (blue) shimming the TF coil bundle to the inner diameter of the OH tension tube to reduce relative motion between the OH and TF coils, (c) amplitude of n=1 vacuum radial magnetic field measured by the upper BR sensors, and (d) toroidal angle of the n=1 vacuum radial magnetic field measured by the upper BR sensors.

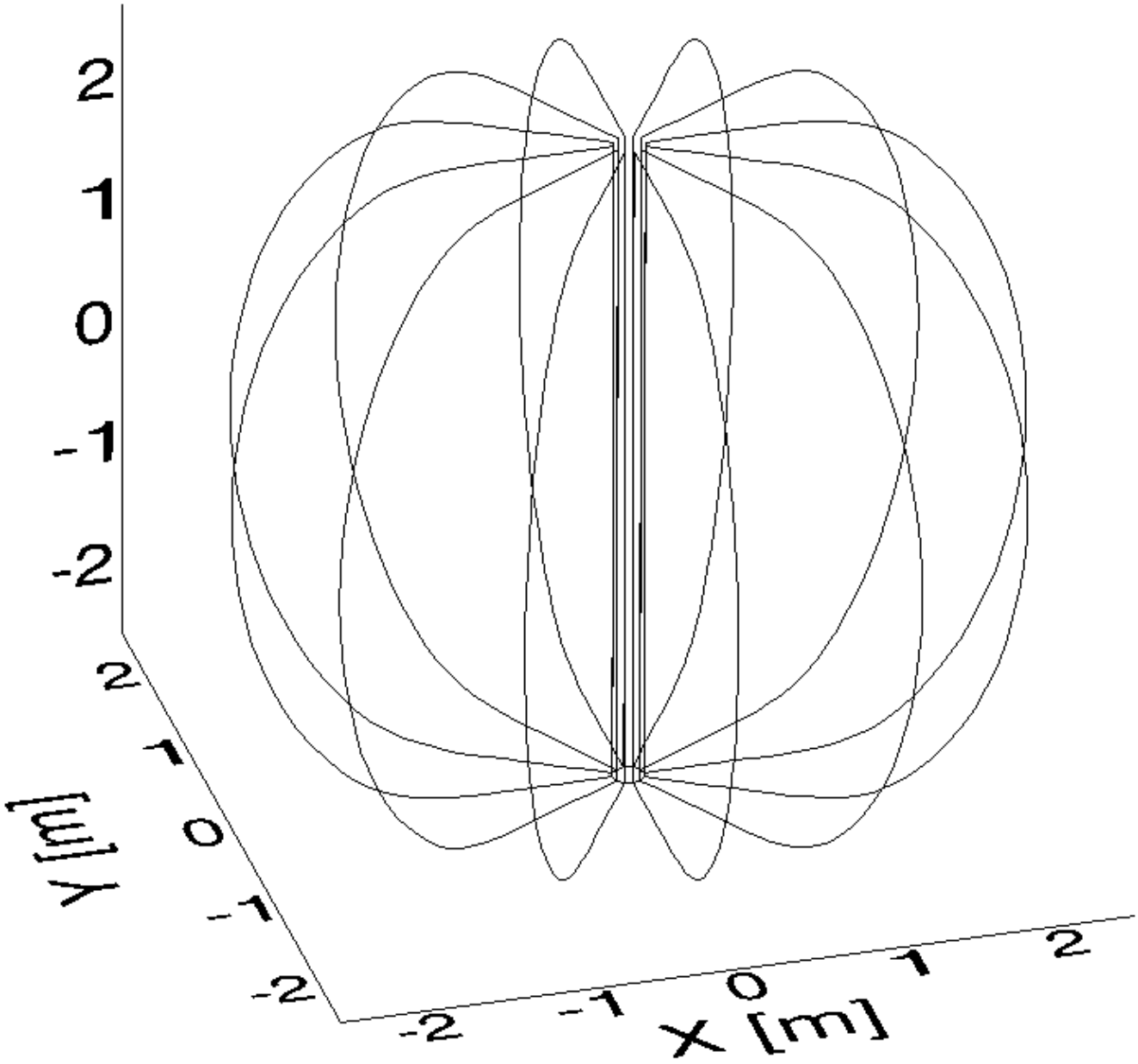

Figure 4. Filamentary model of NSTX toroidal field coils used for calculating error fields from the central toroidal field coil shift and tilt.

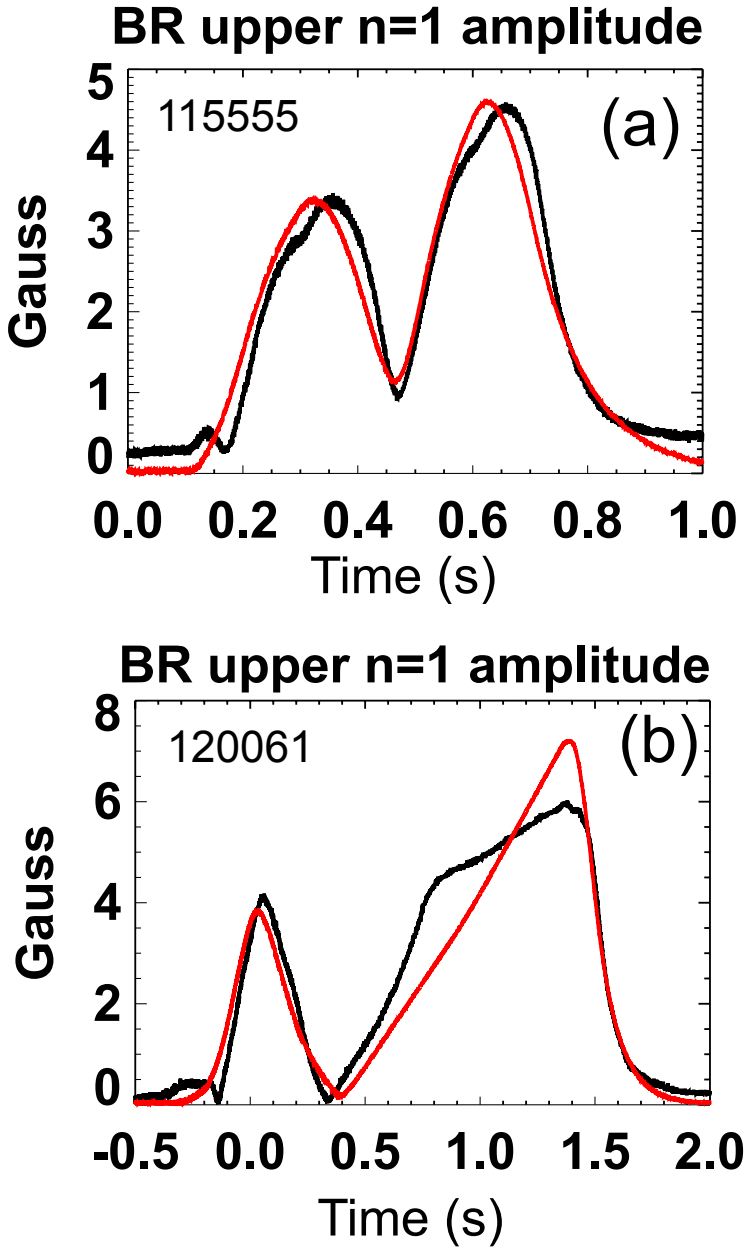

Figure 5. (a) Comparison of measured (black) versus model (red) error field for a shorter duration OH current waveform similar to that used in locked-mode experiments, and (b) comparison of measured (black) versus model (red) error field for the longer duration OH current waveform shown in Figure 3.

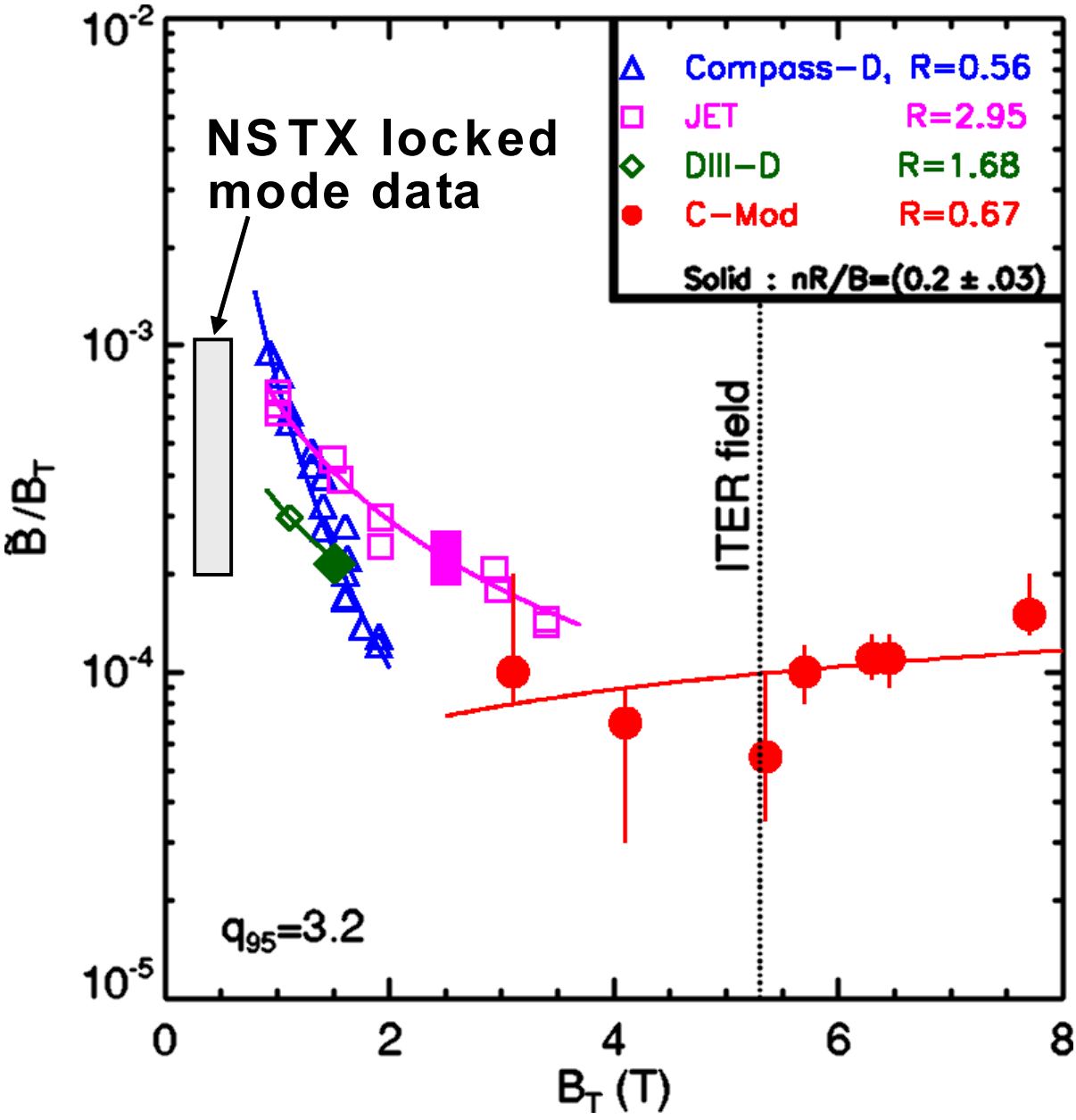

Figure 6. The NSTX locked mode database extends the existing tokamak database to lower toroidal field (0.3-0.55T) as shown by the gray rectangle on the left-hand side of the figure.

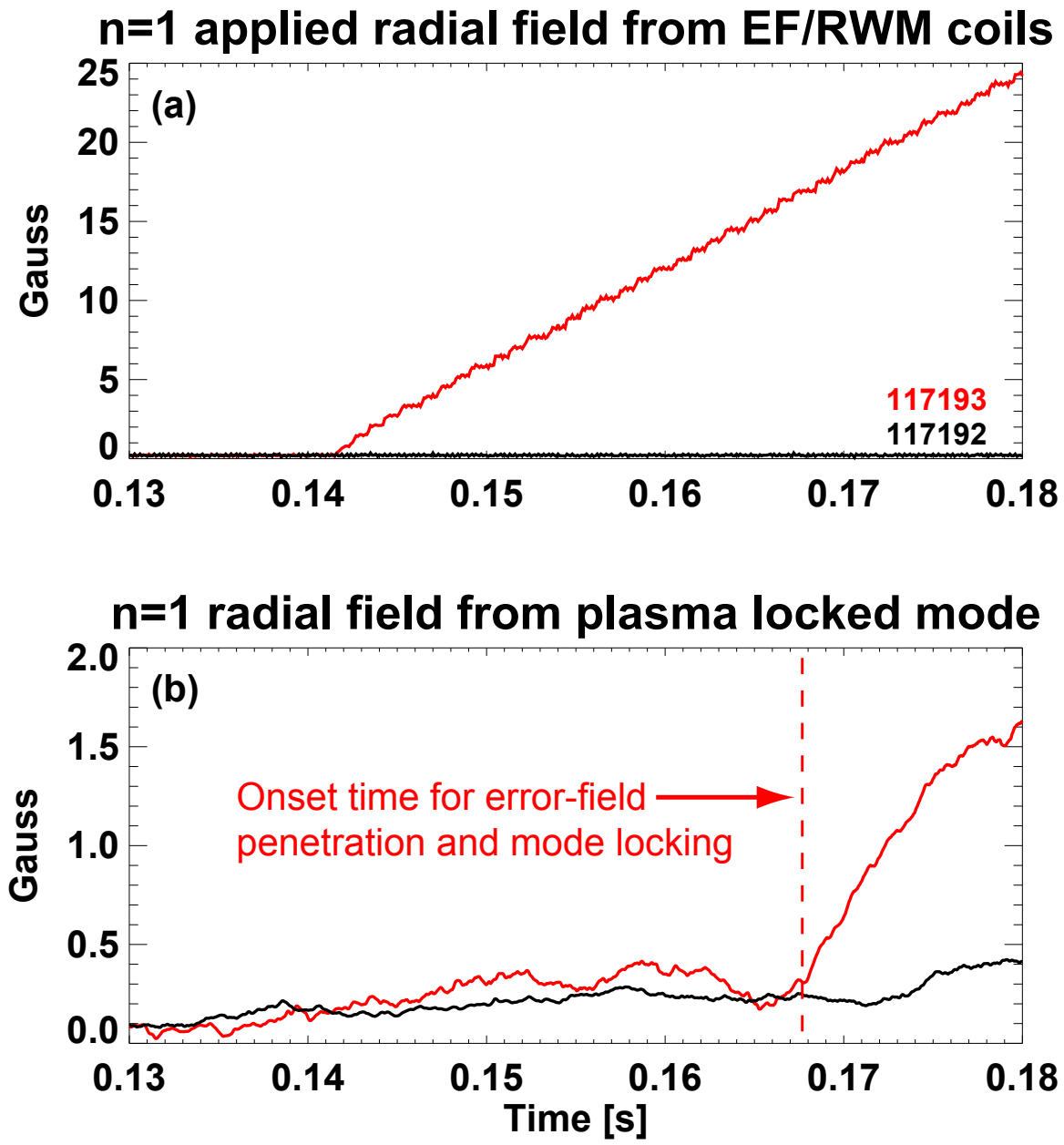

Figure 7. (a) n=1 component of radial magnetic field from the EF/RWM non-axisymmetric field coils measured at the locked-mode sensors, and (b) n=1 component of radial magnetic field from plasma locked mode measured at the locked-mode sensors with (red) and without (black) and applied n=1 time-ramping error-field.

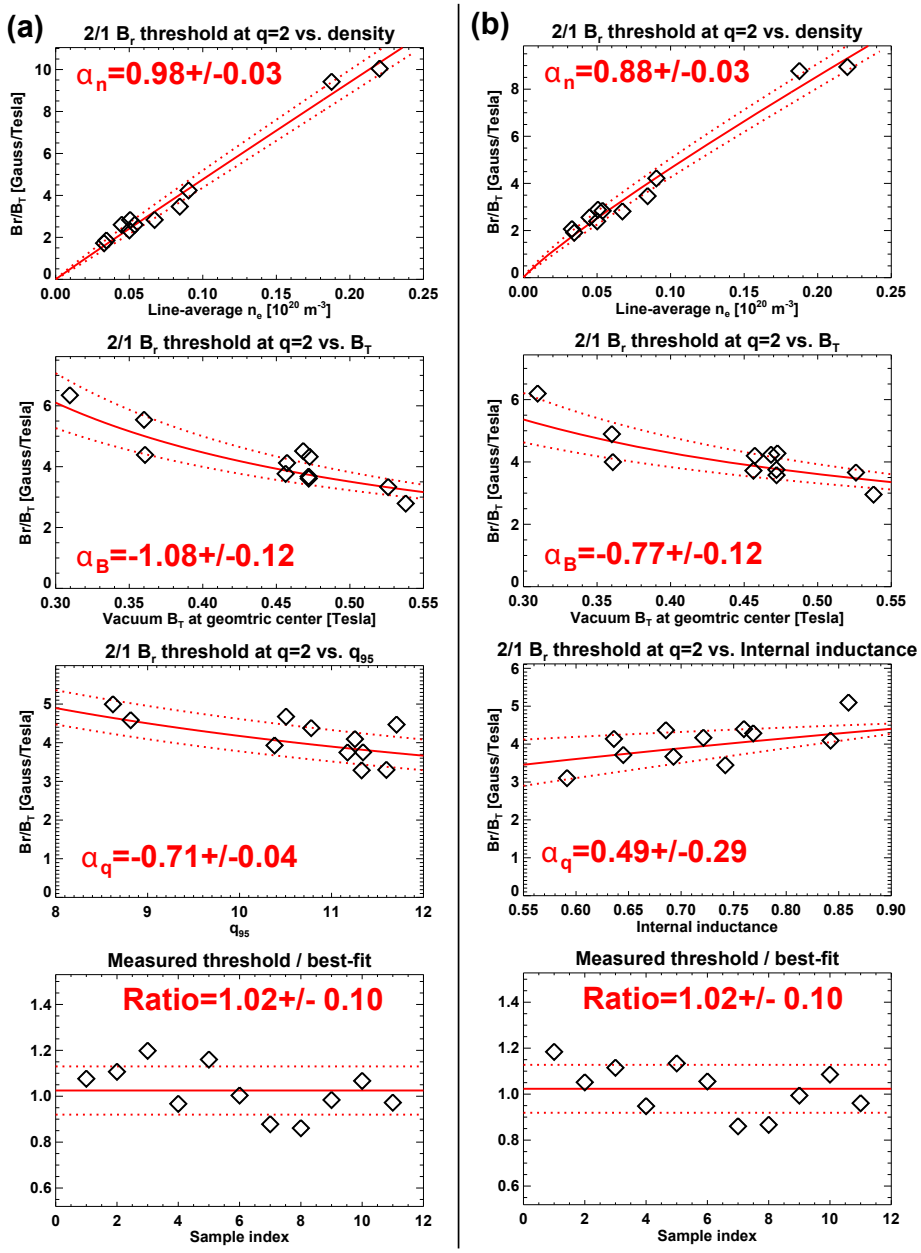

Figure 8. Vacuum superposition m=2, n=1 locked-mode threshold scaling fits to plasma density, vacuum toroidal magnetic field at plasma geometric center, and magnetic safety factor or shear. The left plots (a) use the safety factor computed at the 95% poloidal flux surface as a safety factor variable, whereas the right plots (b) use internal inductance as a magnetic shear variable. The overall fitting errors are shown on the bottom-most plots.

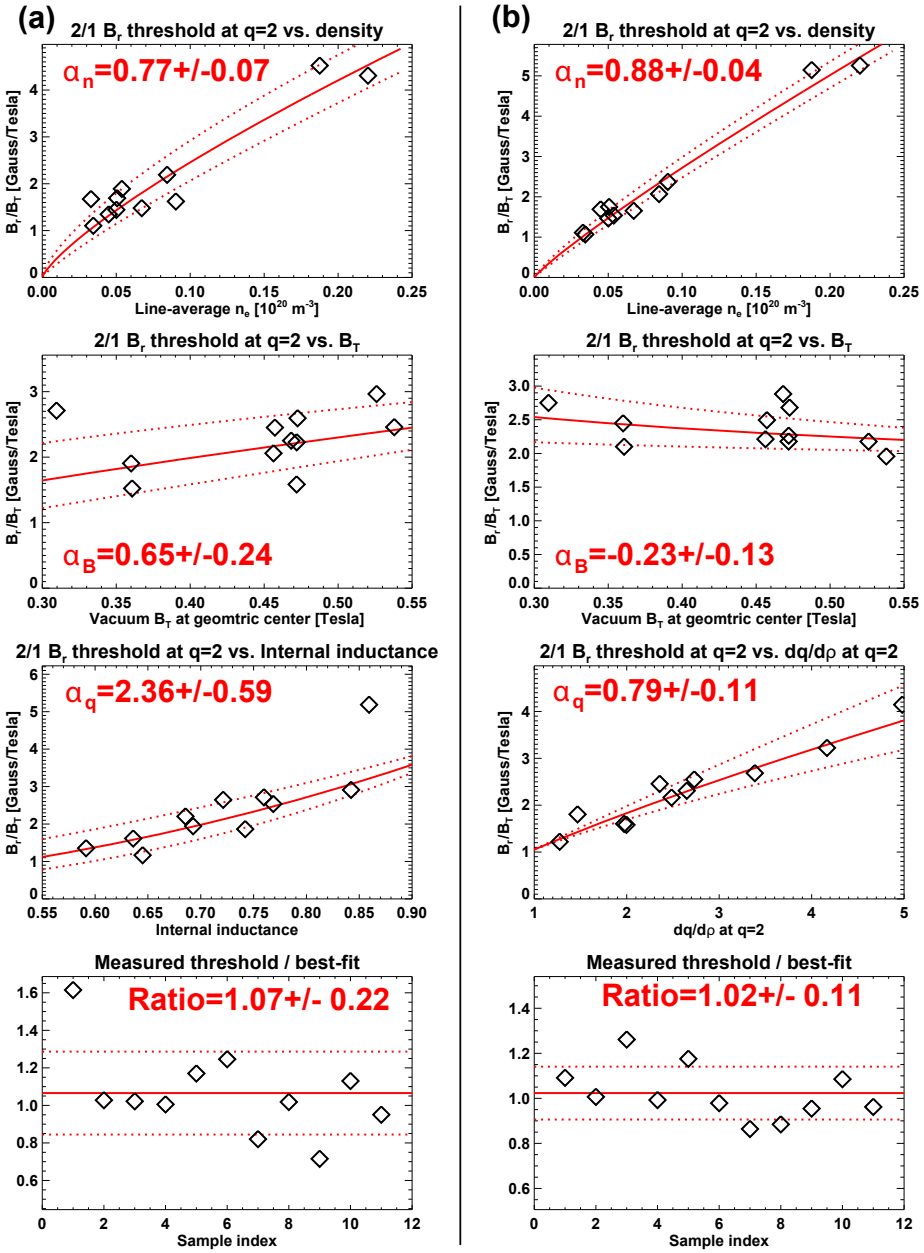

Figure 9. IPEC m=2, n=1 locked-mode threshold scaling fits to plasma density, vacuum toroidal magnetic field at plasma geometric center, and magnetic safety factor or shear. The left plots (a) use the internal inductance as a magnetic shear variable, whereas the right plots (b) use the local magnetic shear at the q=2 surface as a magnetic shear variable. The overall fitting errors are shown on the bottom-most plots.

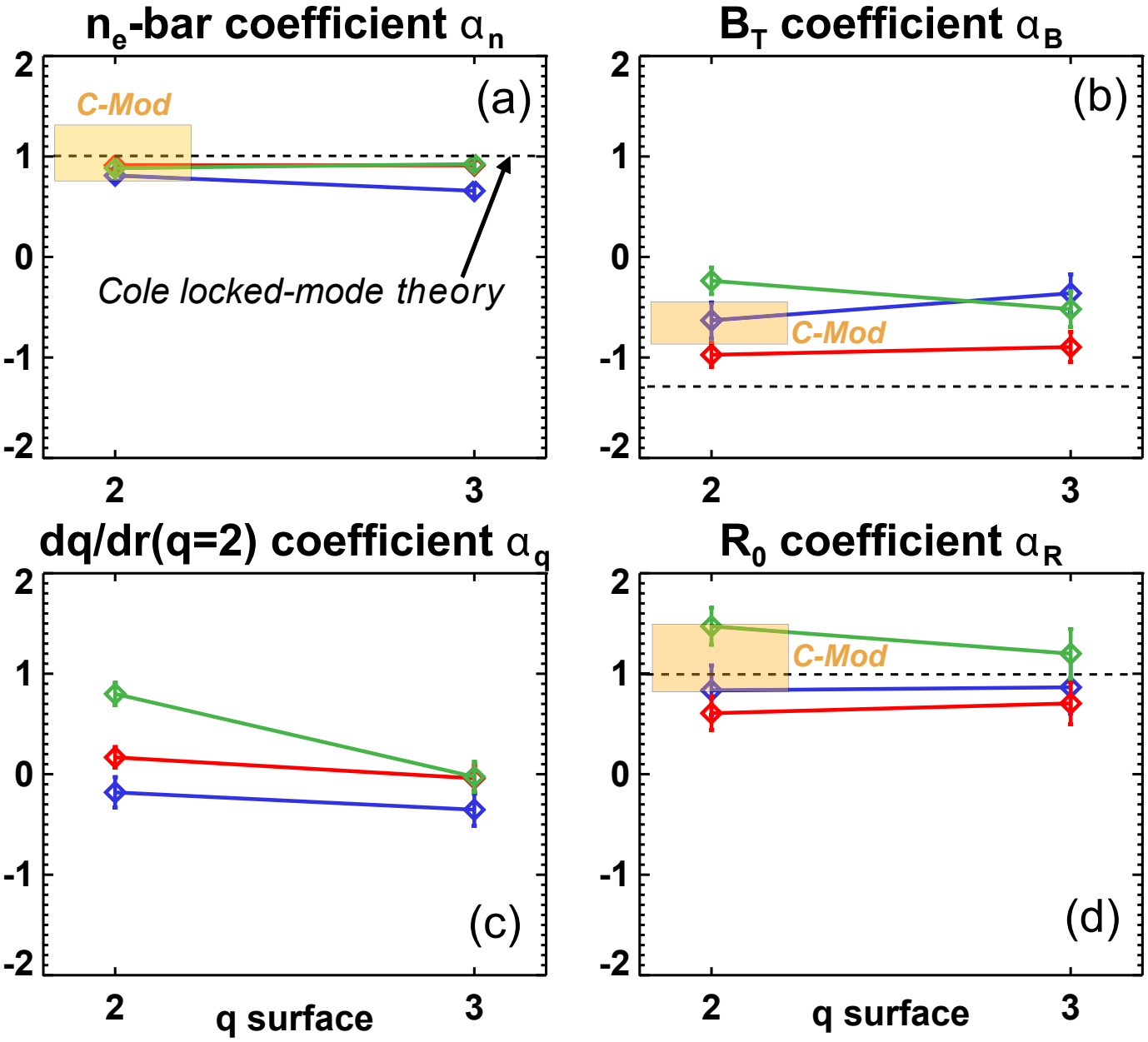

Figure 10. Locked mode threshold scaling exponents for (a) line-average density, (b) vacuum toroidal field at plasma geometric center, (c) magnetic shear at the q=2 surface, and (d) major radius of plasma geometric center.

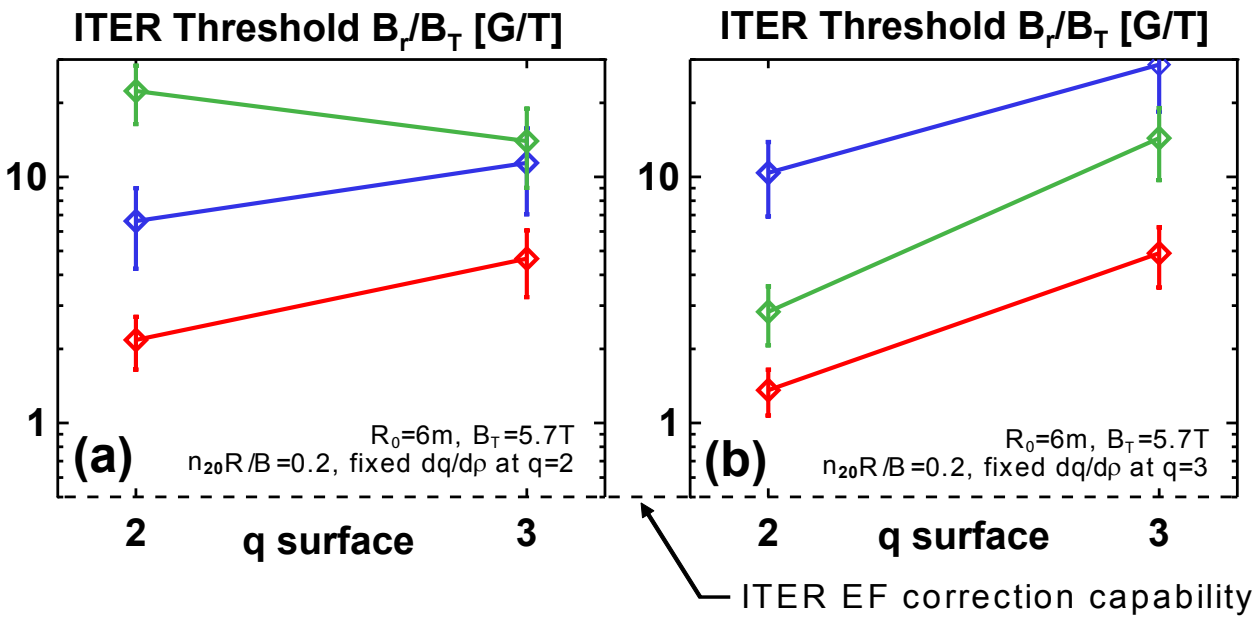

Figure 11. Estimated locked mode threshold for ITER extrapolated from NSTX scaling results using non-area-weighted vacuum field (blue), area-weighted vacuum field (red), and IPEC area-weighted total field (green) for (a) scalings using local shear at the q=2 surface, and (b) scalings using local shear at the q=3 surface. The estimated ITER error-field correction system capability is shown by the dashed line at the bottom of the figure.

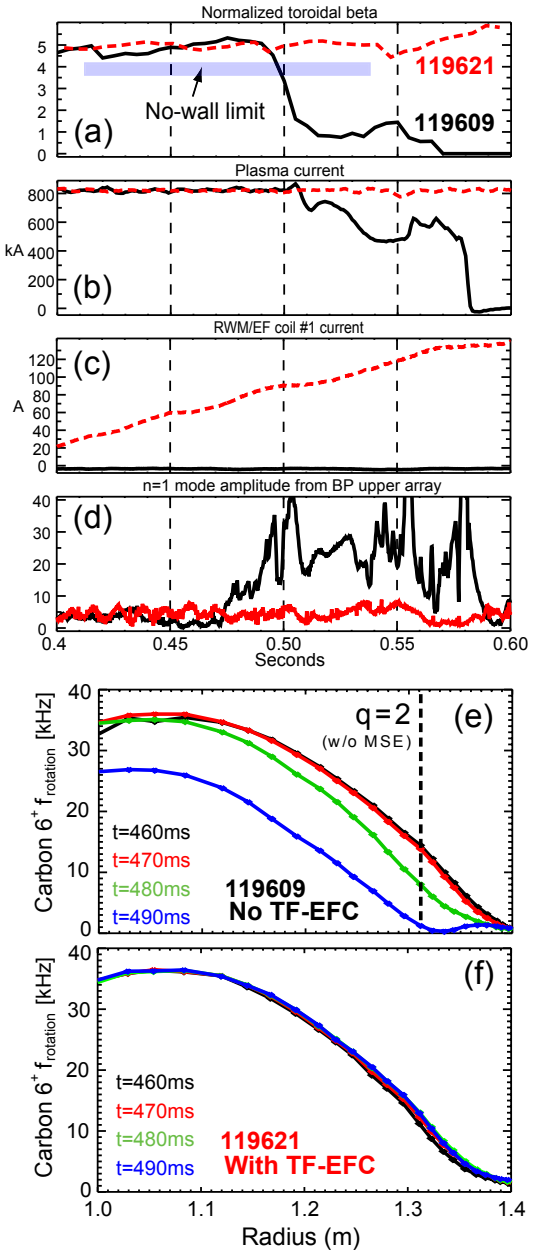

Figure 12. Time evolution of (a) normalized beta, (b) plasma current, (c) RWM/EF coil current, and (d) n=1 mode amplitude for a discharge without (black) and with (red) correction of the n=1 error field from the displaced TF coil shown in Figure 2. Also shown is the time evolution of the plasma rotation profile just prior to the beta collapse (e) without error field correction (EFC), and (f) with TF-EFC.

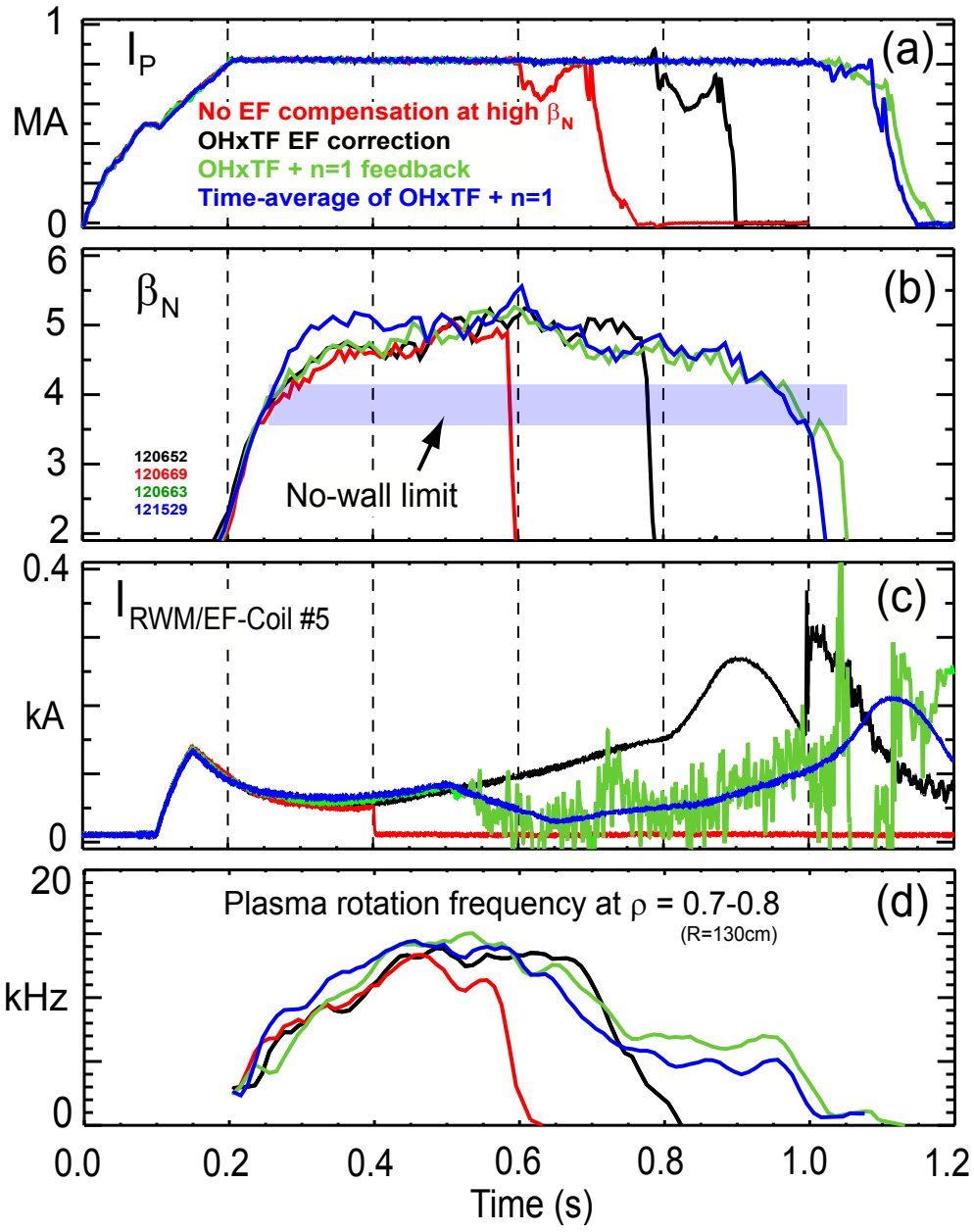

Figure 13. Time evolution of (a) plasma current, (b) normalized beta, (c) RWM/EF coil current, and (d) plasma rotation near the q = 2 and q=3 surfaces during error field correction (EFC) experiments in high beta plasmas.

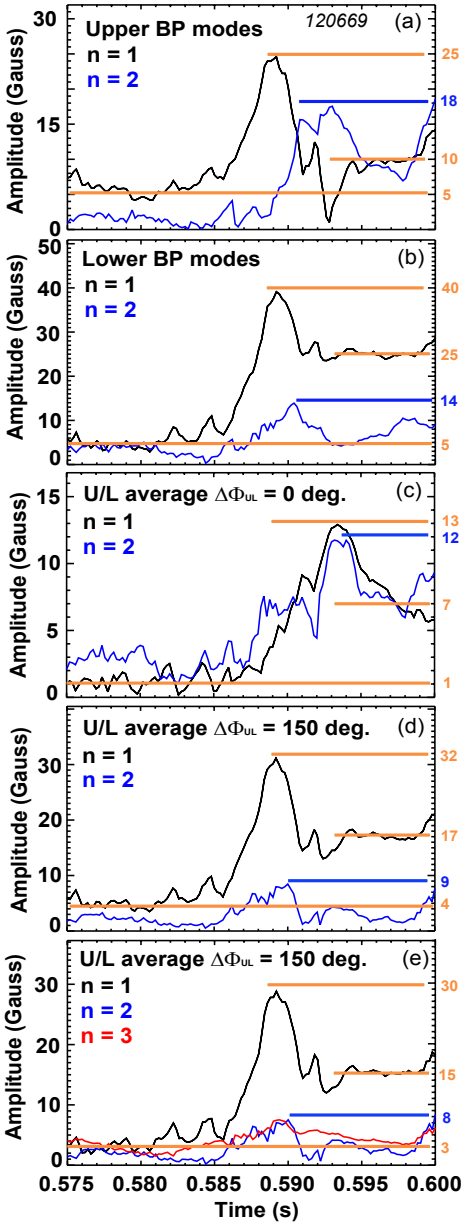

Figure 14. Amplitudes of n=1 (black) and 2 (blue) components of (a) upper (U) BP array, (b) lower (L) BP array, (c) U/L average of BP signals with toroidal phase shift between the upper and lower arrays $\Delta\Phi_{UL} = 0°$, (d) U/L average of BP signals with $\Delta\Phi_{UL} = 150°$ phase shift between U and L arrays, and (e) amplitudes of n=1, 2, and 3 components of U/L average of BP signals with $\Delta\Phi_{UL} = 150°$ phase shift between U and L arrays for shot 120669.

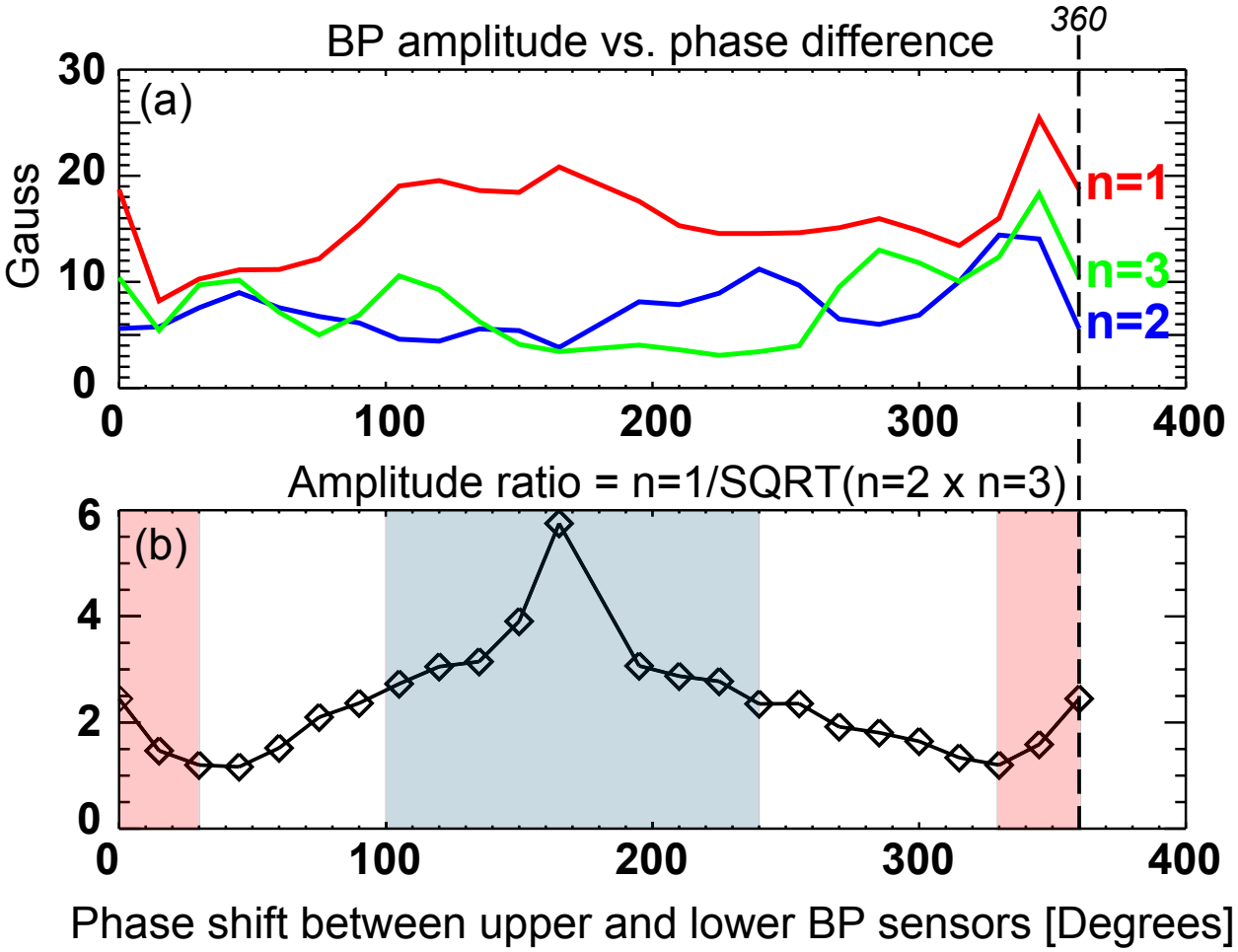

Figure 15. (a) Fourier decomposed amplitudes of toroidal mode number n=1, 2, and 3 components of the upper/lower averaged BP sensor signal versus the toroidal phase shift applied between the upper and lower sensor data, and (b) toroidal mode number amplitude ratio indicating the discrimination of the n=1 component relative to the n=2 and n=3 components versus toroidal phase shift $\Delta\Phi_{UL}$ between upper and lower sensor data for shot 120669 with field amplitudes computed between t=0.585 and 0.600s.

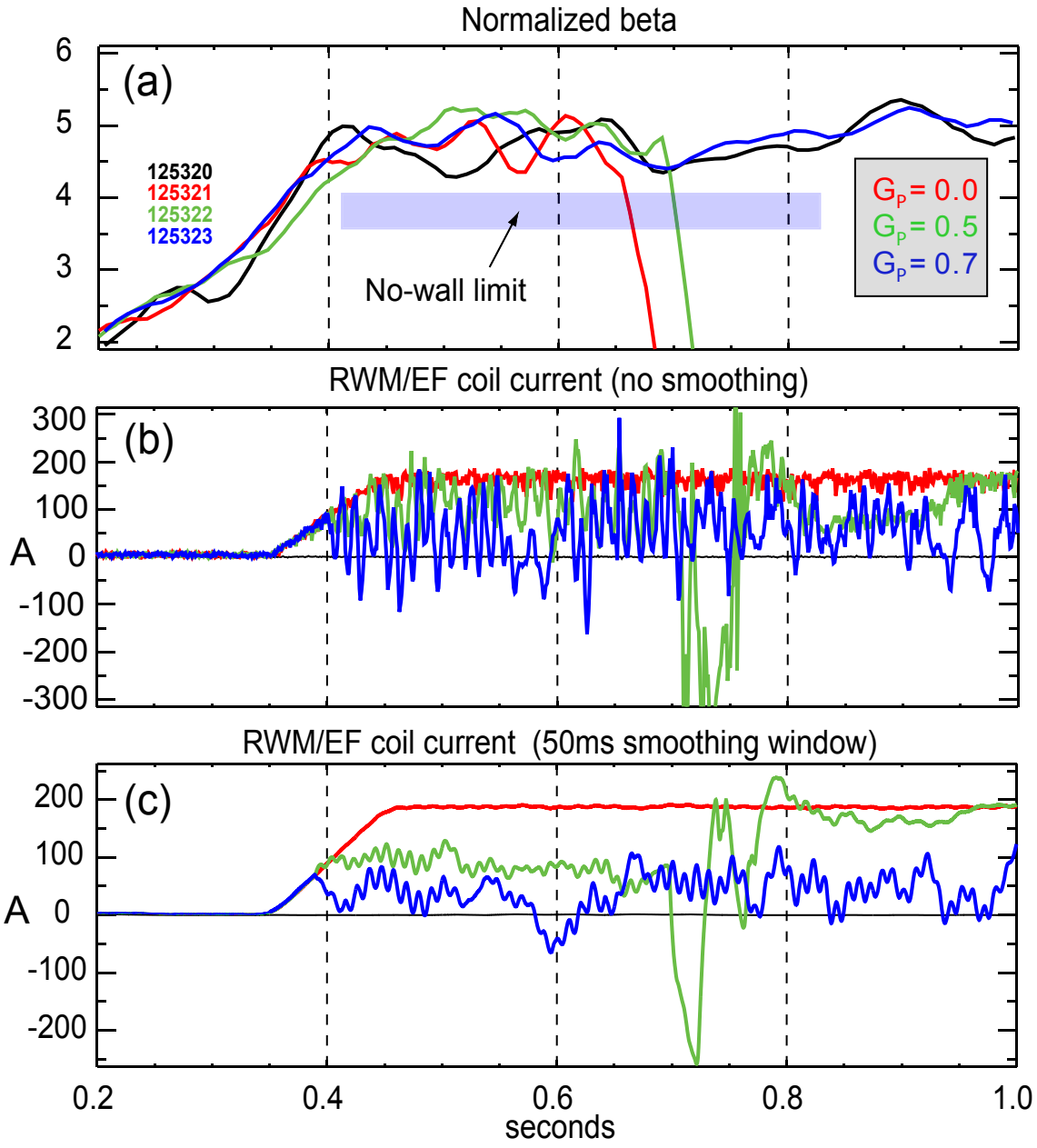

Figure 16. (a) Normalized beta as a function of applied error field and feedback gain during error field suppression experiments designed to optimize error field correction, (b) unfiltered RWM/EF coil current (applied n=1 component plus current from RFA feedback) as a function of applied error field and gain, and (c) filtered RWM/EF coil current using a 50ms smoothing window.

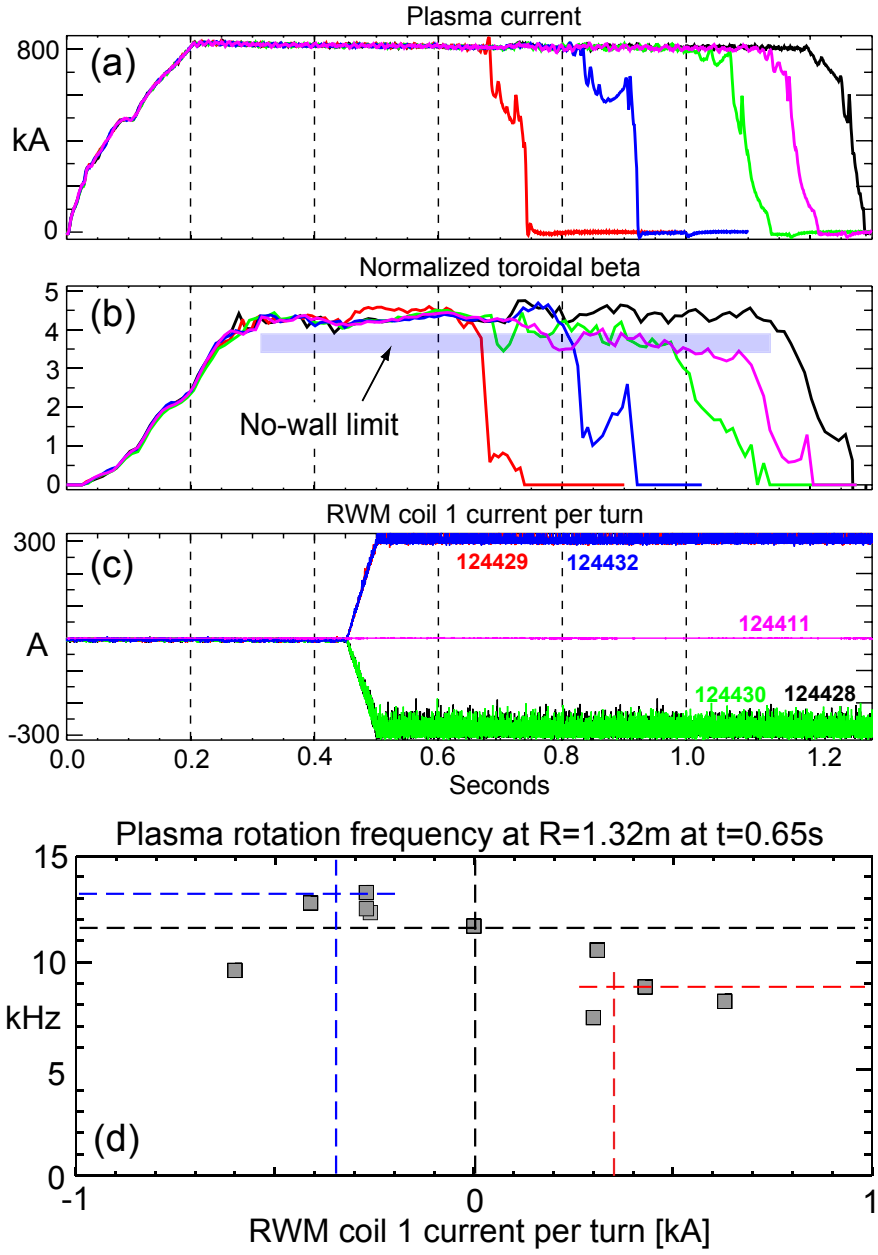

Figure 17. (a) Plasma current, (b) normalized beta, and (c) externally applied n=3 field polarity versus time showing that the maximum plasma pulse-length depends strongly on the direction of applied n=3 field indicating the presence of an n=3 intrinsic error field. A systematic scan (d) of the applied n=3 field amplitude and sign indicates that the plasma pulse-length is maximized for the n=3 current (I_{RWM1} = -0.3kA) which maximizes the plasma rotation frequency at R=1.32m (r/a $\approx$ 0.7) at t=0.65s.

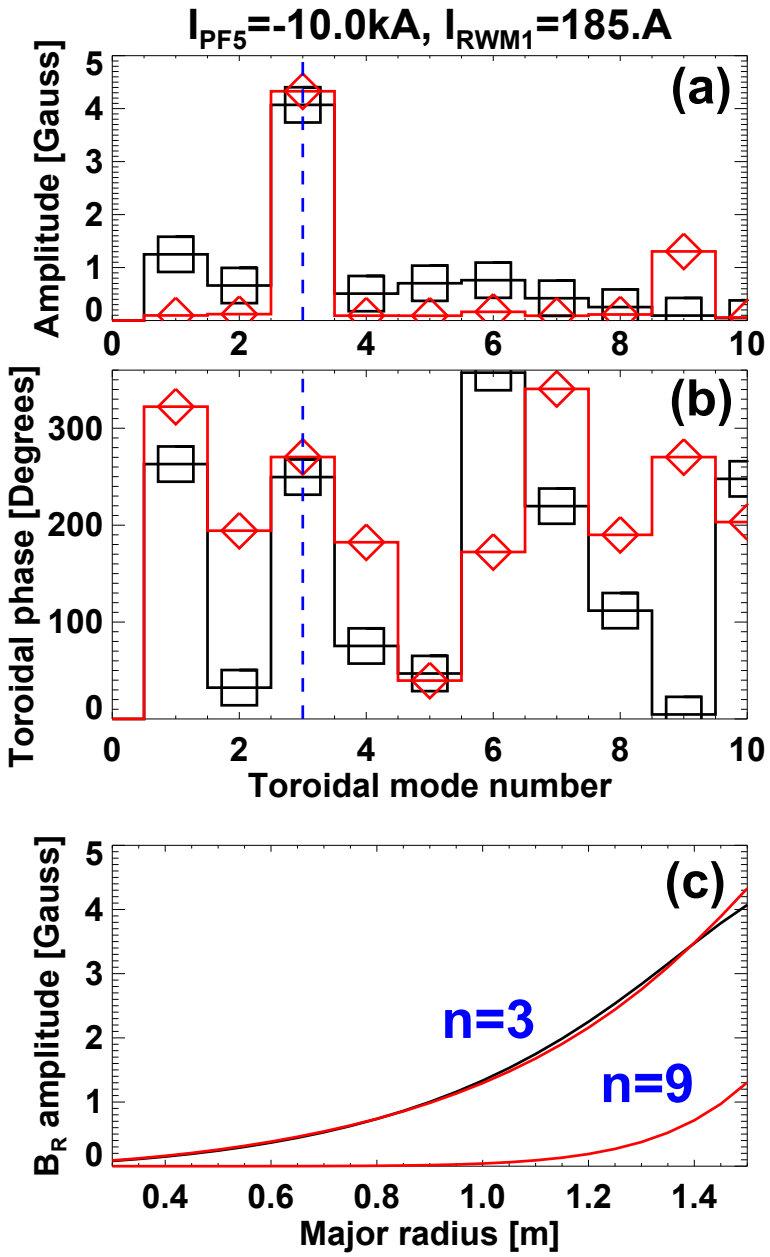

Figure 18. (a) Amplitude and (b) toroidal phase of the non-axisymmetric B_R field component versus toroidal mode number n from the PF5 vertical field coil (black) and the RWM/EF coils for n=3 field (red), and (c) comparison of the radial profiles of B_R at the vertical mid-plane for n=3 and n=9.

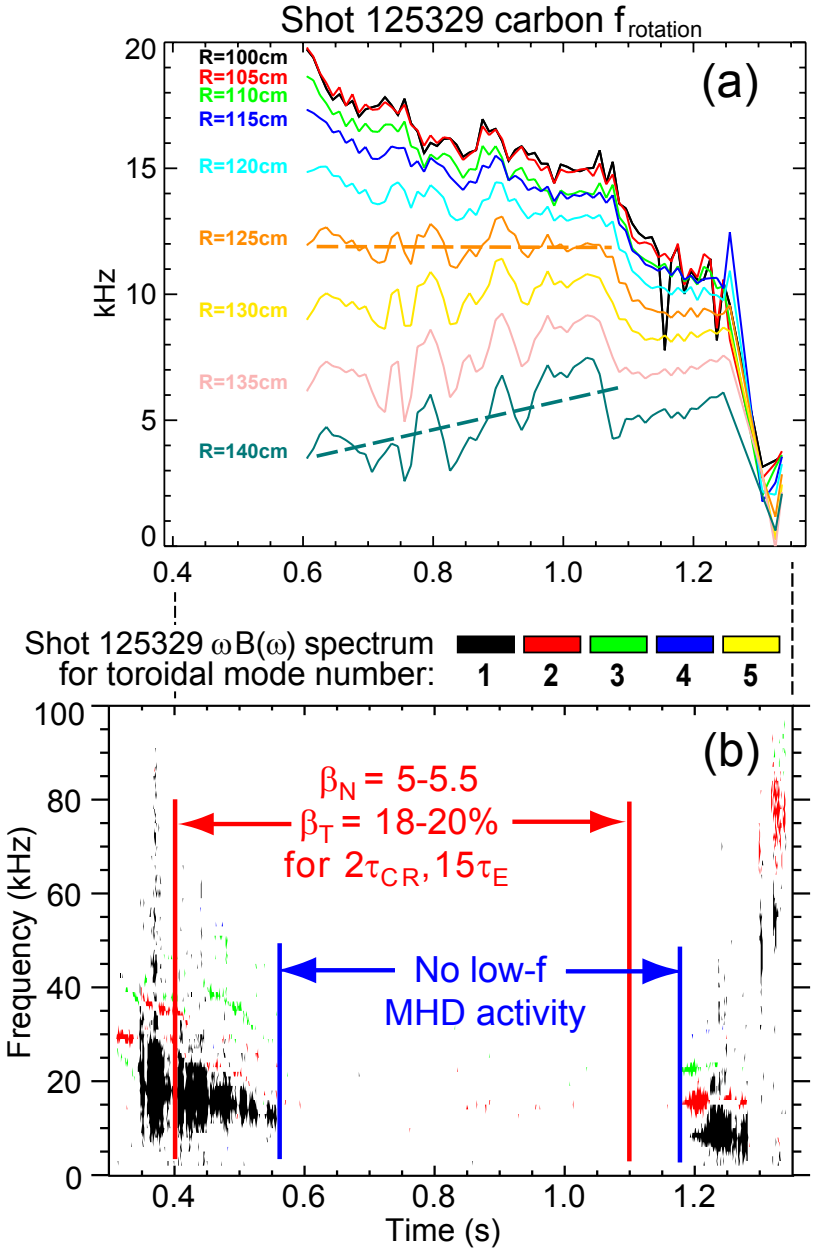

Figure 19. (a) Rotation profile evolution versus time for a discharge with combined optimal n=1 RFA suppression via active feedback (as shown in Fig. 13) and optimal n=3 error-field correction (as shown in Fig. 14). This discharge is unique in that the rotation values for R > 1.25m are constant or increasing as a function of time (until an H-mode to L-mode back-transition at t=1.1s). (b) MHD activity spectrogram showing sustained periods of sustained high-beta and an absence of low frequency MHD activity.

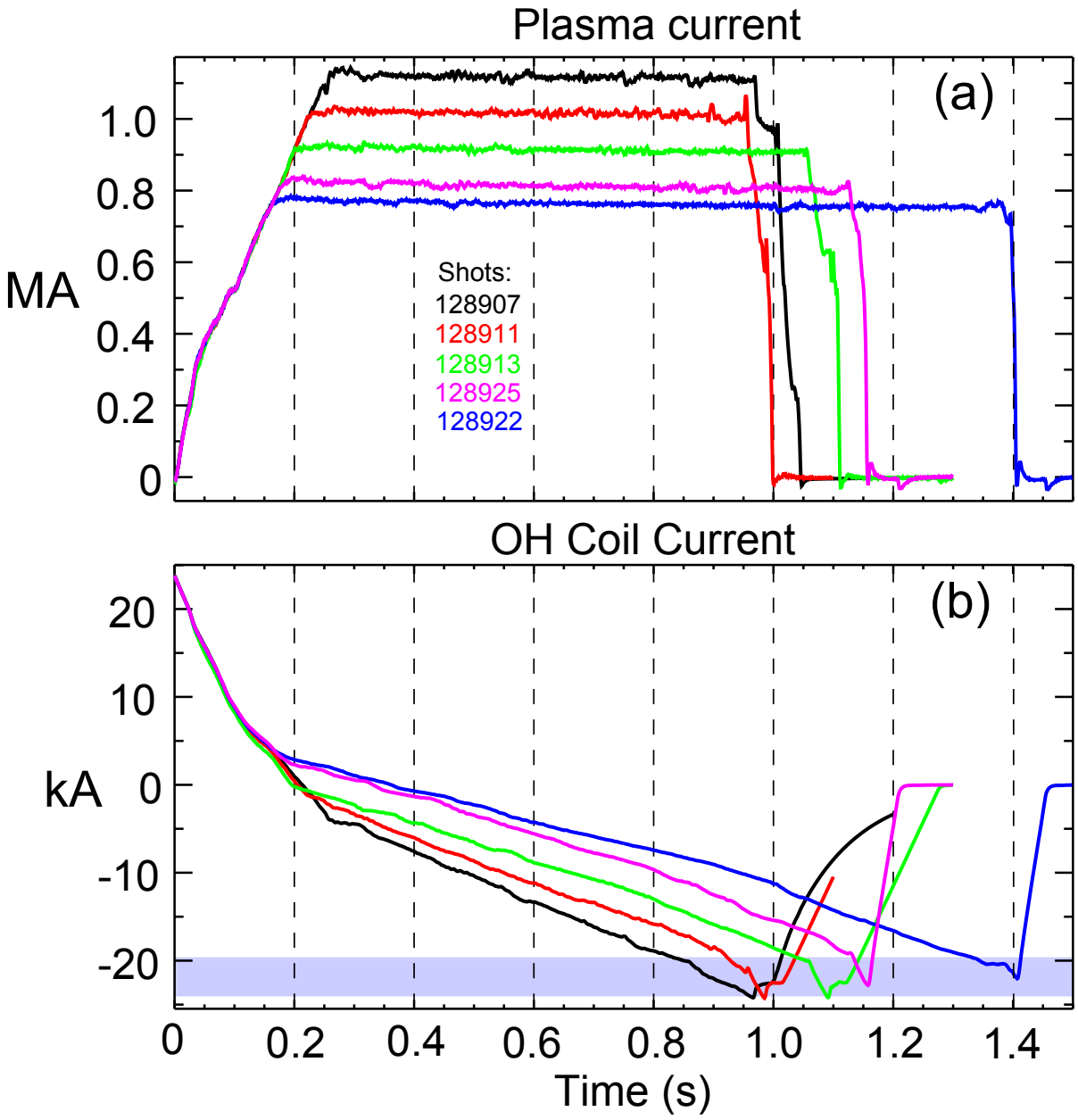

Figure 20. (a) Plasma current waveforms and (b) OH coil current waveforms during a scan of plasma current utilizing optimized n=1 DEFC combined with n=3 EFC.

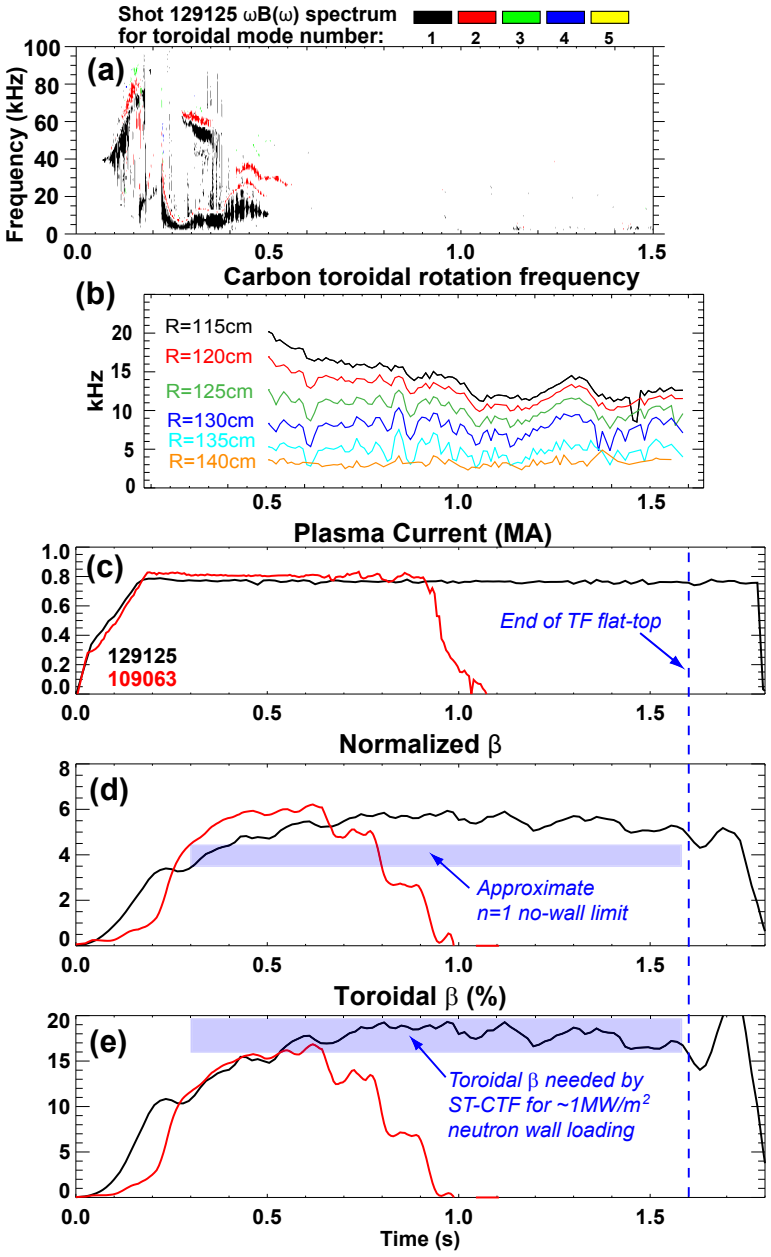

Figure 21. (a) Frequency spectrogram and (b) rotation profile evolution for record pulse-duration plasma on NSTX, and comparison of sustained (c) plasma current, (d) normalized beta, and (e) toroidal beta between present NSTX (black) and NSTX results (from 2002) prior to improvements in plasma shaping, error field control, and Li wall conditioning (red).

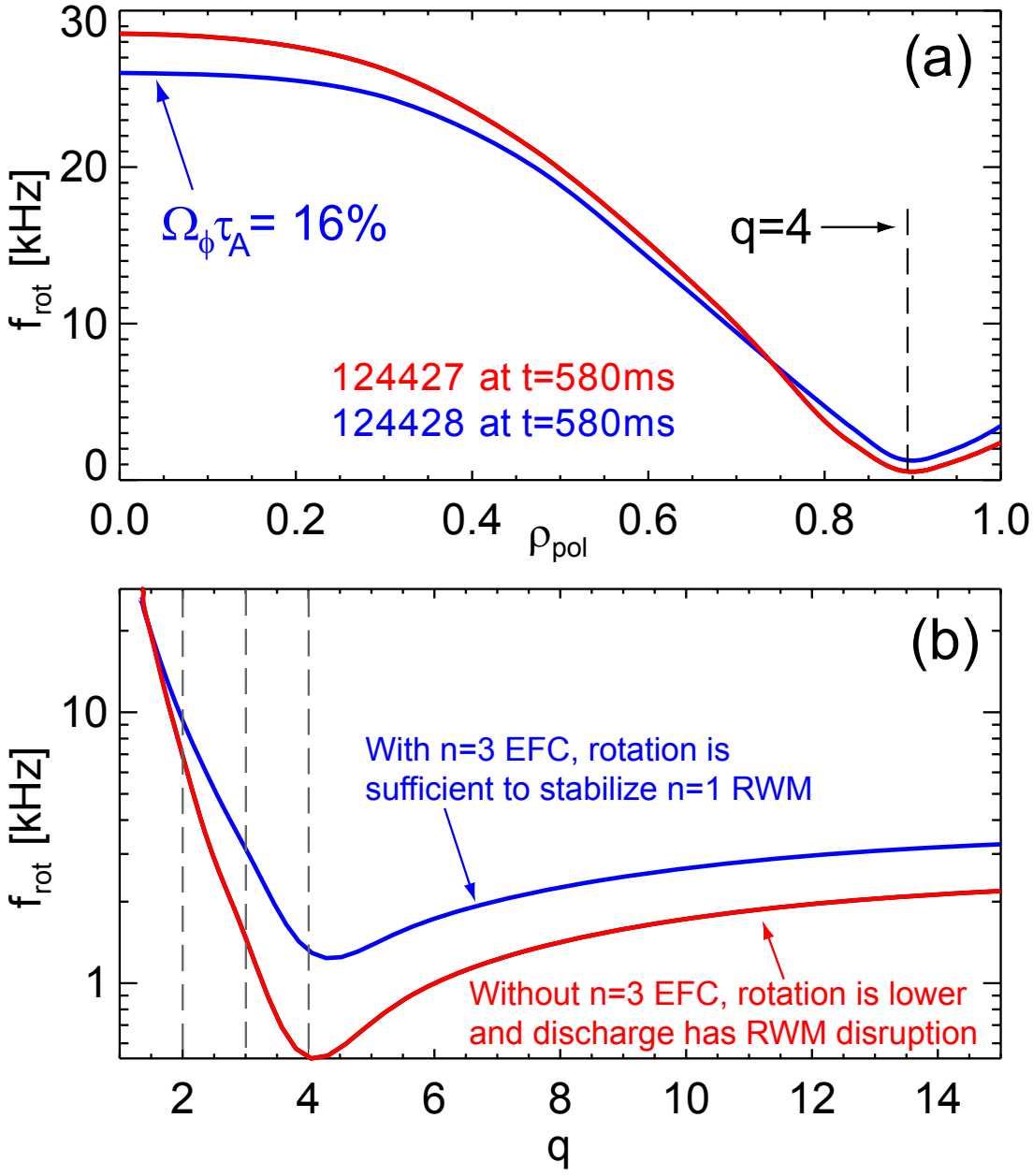

Figure 22. (a) Comparison of plasma rotation profiles versus minor radius for two discharges - one with (blue) and one without (red) n=3 error-field correction (EFC) - at the time (t=0.58s) of n=1 RWM marginal stability for the discharge without EFC. The minimum rotation value occurs near the q=4 surface. (b) Comparison of plasma rotation profiles versus q indicating that the rotation frequency on surfaces with q > 2 apparently determine the n=1 RWM critical rotation for these discharges.

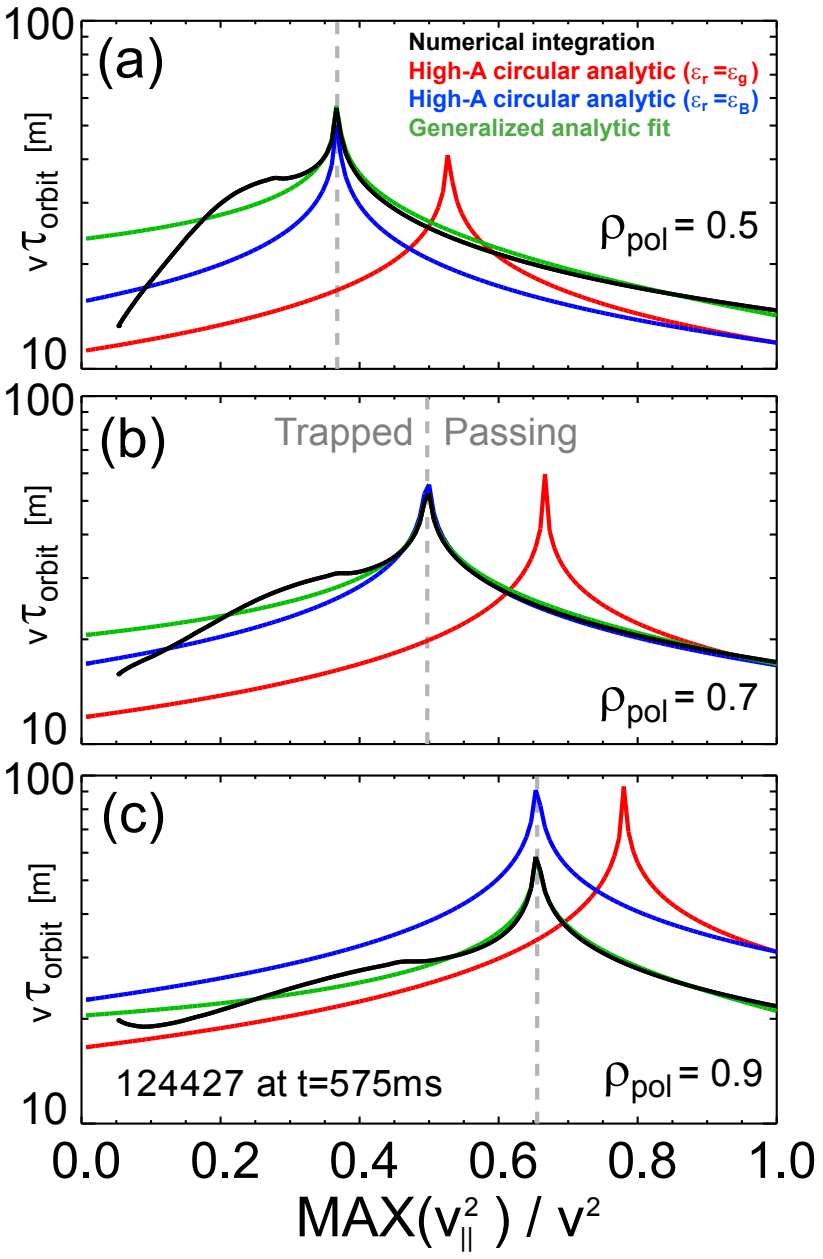

Figure 23. Particle orbit times (trapped and passing) for shot 124427 at t=0.575s as a function of maximum normalized parallel energy (a) near the 1/2 minor-radius ρ_{pol} = 0.5, (b) near the q=2 surface at ρ_{pol} = 0.7, and (c) near the q=4 surface closer to the plasma edge at ρ_{pol} = 0.9.

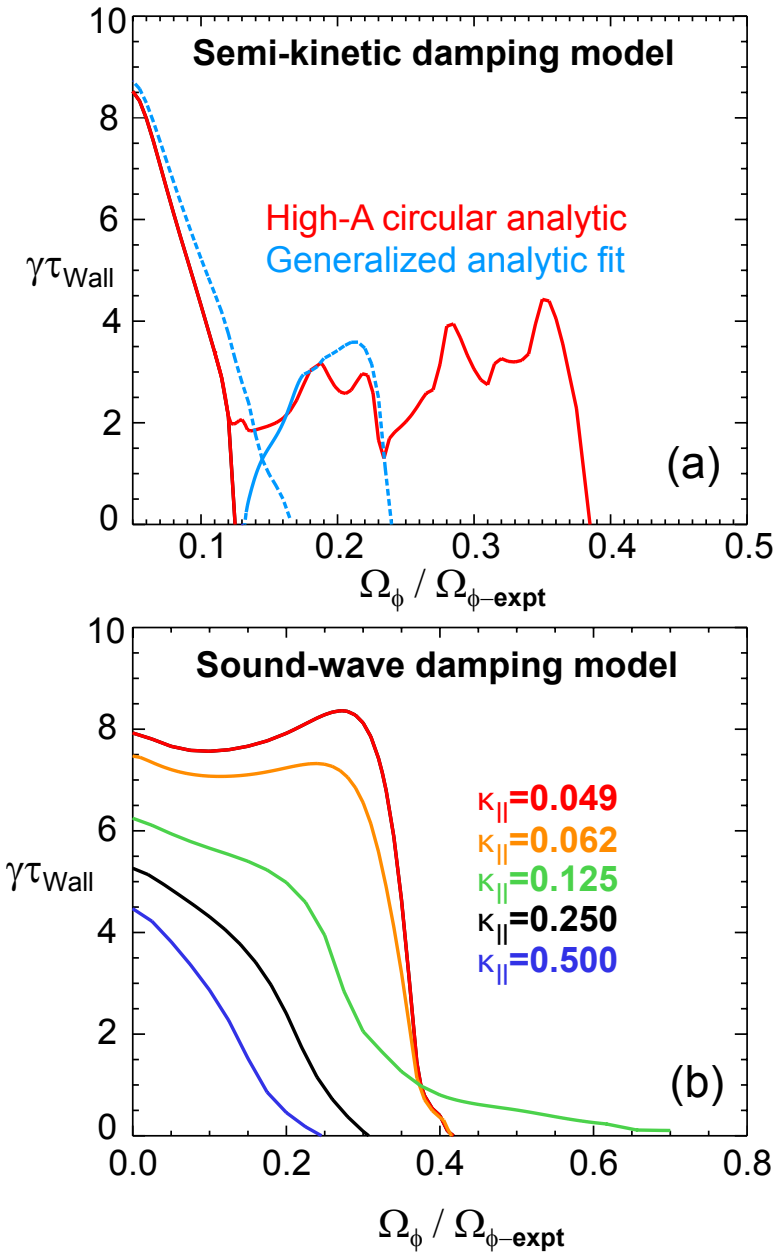

Figure 24. (a) MARS-F semi-kinetic damping model predictions of the RWM growth rate using the high-A circular cross-section ($\epsilon_r = \epsilon_g$) approximation for the particle orbit times (red) and the general-geometry analytic fit to the particle orbit times (blue). (b) MARS-F sound-wave damping model predictions of the RWM growth rate for different Landau damping multipliers.

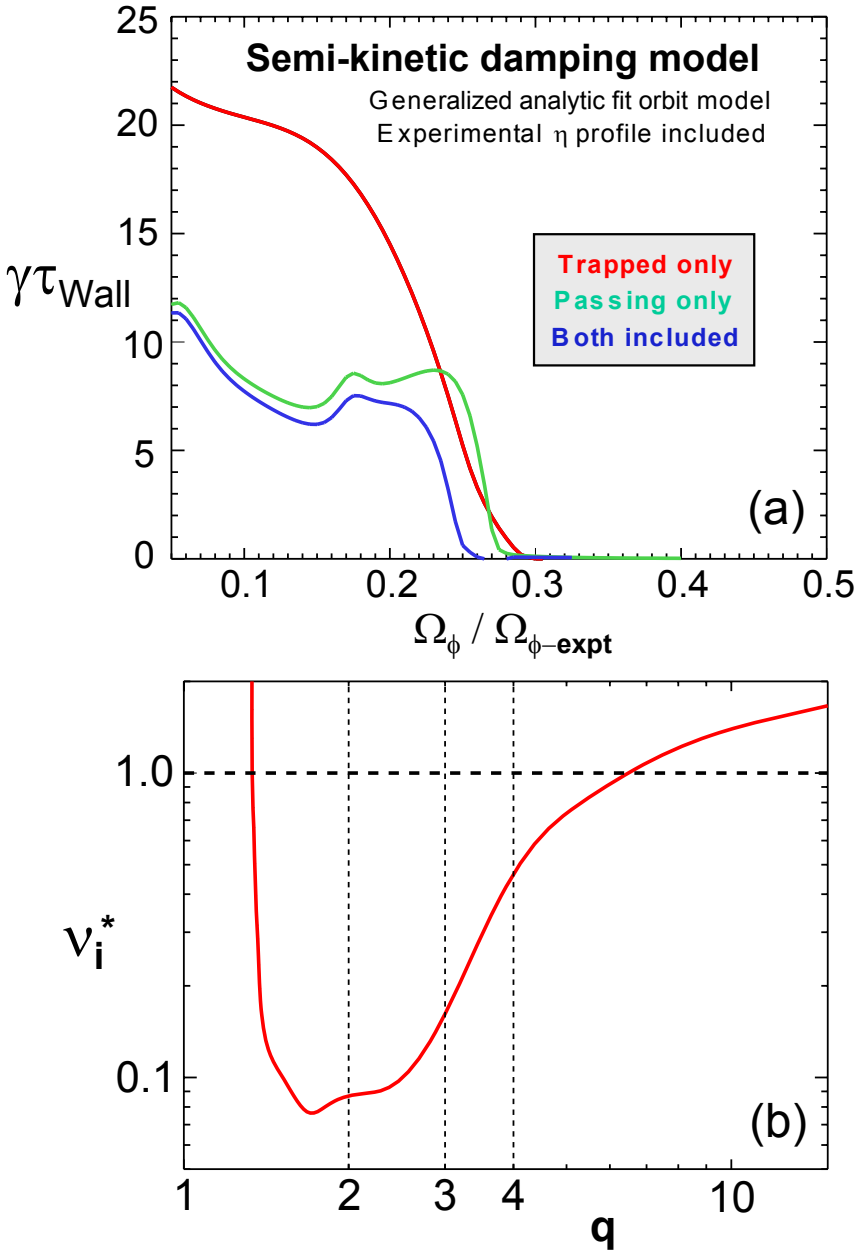

Figure 25. (a) Growth rate of the n=1 RWM computed with the MARS-F code plotted versus plasma rotation using the generalized-geometry analytic fit to the particle orbit times and including the neoclassical parallel resistivity profile for the plasma resistivity. (b) Profile of ν_i^* versus q for the same discharge.

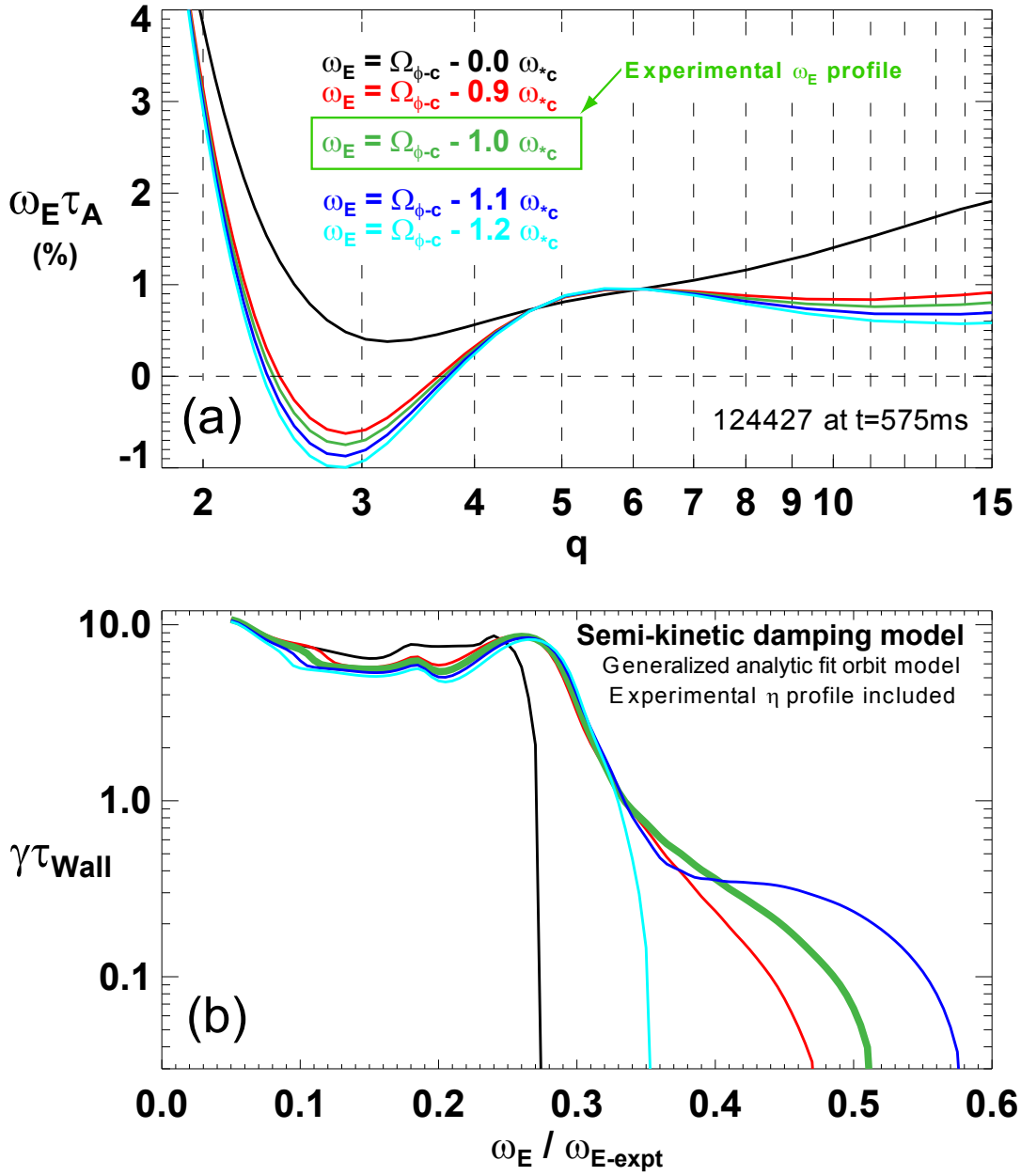

Figure 26. (a) Comparison of plasma ω_E profiles versus q for the RWM unstable plasma excluding (black) and including (other colors) the carbon impurity diamagnetic rotation in the radial force balance equation for the calculation of the electrostatic potential profile $\Phi(\psi)$. (b) Comparison of growth rates of the n=1 RWM computed with the MARS-F code plotted versus ω_E using the generalized-geometry analytic fit to the particle orbit times and including the neoclassical parallel resistivity profile for the plasma resistivity.

The Princeton Plasma Physics Laboratory is operated
by Princeton University under contract
with the U.S. Department of Energy.

Information Services
Princeton Plasma Physics Laboratory
P.O. Box 451
Princeton, NJ 08543

Phone: 609-243-2245
Fax: 609-243-2751
e-mail: pppl_info@pppl.gov
Internet Address: http://www.pppl.gov